RUPRECHT-KARLS-UNIVERSITÄT HEIDELBERG

Alexander Tadday

Characterisation of Silicon Photomultipliers

Diploma Thesis

HD-KIP-08-18

KIRCHHOFF-INSTITUT FÜR PHYSIK

Faculty of Physics and Astronomy

University of Heidelberg
Diploma thesis
in Physics
submitted by
Alexander Tadday
born in Ludwigsburg
2008

Characterisation of Silicon Photomultipliers

This diploma thesis has been carried out by Alexander Tadday at the
Kirchhoff Institute for Physics
under the supervision of
Prof. Dr. Hans-Christian Schultz-Coulon

Abstract

This thesis describes the development and construction of a test-setup to determine the characteristic properties of *Silicon Photomultipliers* (SiPMs). Furthermore, the application of SiPMs for the *Positron Emission Tomography* (PET) imaging technique was studied.

The highly granular hadronic calorimeter prototype, developed in preparation for the *International Linear Collider* (ILC), utilises SiPMs for the measurement of light produced by small scintillating tiles. Systematic studies have been performed in this work, including measurements of gain, dark-rate and photon detection efficiency which allow to compare SiPMs from different manufacturers. These studies are helpful in order to select a specific device for future prototypes and for the final detector design.

Complementary to the characterisation, a test-setup was built using *Multi-Pixel Photon Counters* (MPPCs) in order to test their applicability to PET. Values for the relative energy resolution of $(10 \pm 0.3)\,\%$ and for the timing resolution of $(578 \pm 35)\,\mathrm{ps}$ were measured with LSO used for the scintillating material. These values are comparable to typical values obtained by photomultipliers.

Zusammenfassung

Diese Arbeit beschreibt die Entwicklung und den Aufbau eines Testsystems zur Bestimmung der charakteristischen Eigenschaften von *Silizium Photomultipliern* (SiPMs) und deren Anwendbarkeit für das bildgebende Verfahren der *Positronen Emissions Tomographie* (PET).

Der hoch granulare Prototyp des hadronischen Kalorimeters, der im Rahmen der Vorbereitungen für den *International Linear Collider* (ILC) entwickelt wurde, verwendet SiPMs zum Nachweis von Licht das von kleinen Szintillatorkacheln erzeugt wird. Systematische Messungen des Gains, der Dunkelrate und der Photon-Detektionseffizienz wurden im Rahmen dieser Arbeit durchgeführt, die es ermöglichen SiPMs unterschiedlicher Hersteller zu vergleichen. Diese Untersuchungen sind hilfreich um eine Auswahl für zukünftige Prototypen und für den endgültigen Detektorentwurf zu ermöglichen.

Ergänzend zur Charakterisierung wurde unter Verwendung von *Multi-Pixel Photon Counters* (MPPCs) ein weiterer Testaufbau errichtet, mit dessen Hilfe ihre Anwendbarkeit für PET-Systeme überprüft werden konnte. Werte für die relative Energieauflösung von $(10 \pm 0,3)\,\%$ und für die Zeitauflösung von $(578 \pm 35)\,\mathrm{ps}$ wurden gemessen, unter Verwendung von LSO als Szintillatormaterial. Diese Werte sind vergleichbar mit typischen Werten ermittelt mit Photomultipliern.

Contents

Chapter 1

Introduction

During the last century many experimental results gave rise to the formation of the *Standard Model* (SM) which successfully describes all measurements in the field of particle physics. It describes the interactions between the elementary particles and was also successful in the prediction of new particles which later on could be found with detectors at large particle accelerators. One of the main objectives of current experiments is the search for the Higgs particle, a predicted component of the SM which hasn't been observed yet. It could explain the observation of particle masses and the breaking of the electroweak force.
Electroweak precision measurements from previous experiments at LEP[1], SLC[2] and Tevatron provide indirect sensitivity to the Higgs mass and yield a value of $m_h = 85^{+39}_{-28}\,\mathrm{GeV}$, giving an upper limit for the Higgs mass m_h of 166 GeV at a confidence level of 95%.
A long planned research project will soon be completed at the *European Organisation for Nuclear Research* (CERN)[3], the *Large Hadron Collider* (LHC). It will collide protons with a maximum centre of mass energy $\sqrt{\mathrm{s}} = 14\,\mathrm{TeV}$ and therefore most probably discover the Higgs particle, or particles predicted by alternative theories (e.g. supersymmetry) in case they have masses below a few TeV. The spectrum of possible physics at this energy-scale is multi-facetted, therefore the demands to the detectors will be exceptional. However the LHC is colliding protons, consisting of quarks and gluons; the knowledge about the colliding partons is therefore limited compared to a lepton collider with a well defined initial state. For precision measurements of the discovered physics like precise measurements of the Higgs properties in consequence an electron positron collider would be needed.
The proposed accelerator for this purpose is the *International Linear Collider* (ILC). It is designed as a superconducting linear collider accelerating electrons and positrons with a centre of mass energy ranging from $\sqrt{s} = 200$ GeV to $\sqrt{s} = 500$ GeV for high luminosity physics runs. The present design even includes the possibility of an upgrade to $\sqrt{s} = 1\,\mathrm{TeV}$ [1].
Even though the demands for the detector in terms of event rates, background and radiation hardness are weaker compared to the LHC, the ILC will investigate physics placing challenging demands on the precision of measurements of particle tracking and identification. To achieve separation between events containing two W or two Z bosons which is crucial for many interesting physics channels, the energy resolution of such a detector for hadronic jets has to reach $30\%/\sqrt{E_{jet}}$ which is a factor of two better than the best achieved so far. This could be achieved with an excellent tracking system in combination with a calorimeter with very fine transverse and longitudinal segmentation utilising a new reconstruction method, the so-called *Particle Flow Approach* (PFA).

---

[1] Large Electron Positron Collider

[2] Stanford Linear Collider

[3] French: Conseil Européen pour la Recherche Nucléaire

Within the CALICE[4] collaboration several concepts for the electromagnetic and the hadronic calorimeters are proposed. A unique approach for the hadronic calorimeter is a fine segmented sandwich structure consisting of alternating layers of steel and plastic scintillator in the shape of small $3 \times 3 \times 0.5\,\mathrm{cm}^3$ tiles. A prototype of this calorimeter has been built at the *German Electron Synchrotron* (DESY)[5] to study the applicability of this concept. The scintillation light is read out with a novel kind of silicon photodetector, the so-called *Silicon Photomultiplier* (SiPM). Due to the exceptional properties of this device like high gain, compactness and insensitivity to magnetic fields they are well suited for this application and are also studied for a tailcatcher and muon tracker system.

A similar device, the *Multi Pixel Photon Counter* (MPPC), is studied for an electromagnetic calorimeter also utilising plastic scintillator, but with higher granularity compared to the hadronic calorimeter and tungsten as absorber. However, the MPPC could be used also for the hadronic calorimeter in the future. The growing variety of available devices belonging to this family requires the possibility to test and to characterise them in order to support the selection procedure for a final design. Therefore a test setup was built in the context of this thesis in order to measure the characteristics of the devices and to compare them.

The application of the SiPM is not limited to the field of high energy physics. Moreover it can be used for all applications where the above mentioned properties are needed. As it was reviewed in [2, 3] there are many synergies between high energy physics and the field of medical imaging. This means that parts of the technology used are similar and can be adopted from one application to the other, e.g in the case of *Positron Emission Tomography* (PET), a medical imaging technique which utilises photons resulting from positron annihilation to generate a three-dimensional image of a body. Traditionally these photons are detected by a detector consisting of an inorganic scintillator, read out by photomultiplier tubes. The same advantages of the SiPM mentioned for calorimetry make it a promising candidate for PET. Especially the combination of PET with the *Magnetic Resonance Imaging* (MRI) technique would add some high advantages for medical imaging, since both techniques provide a different view of the body which complement each other. Until now this was not possible with photomultipliers because of their sensitivity to magnetic fields. Therefore the SiPM was studied in this thesis besides the general characterisation as a potential readout for PET.

---

[4] Calorimeter for the Linear Collider Experiment

[5] German: Deutsches Elektronen Synchrotron

1.1 The International Linear Collider (ILC)

The ILC will be the next big particle accelerator project after the LHC which is currently being built in the tunnel of the former LEP collider at CERN. The LEP experiments have demonstrated the advantages of an e^+e^- collider, like the high precision achievable in the determination of particles masses. A total energy of 209 GeV was finally reached. However an energy upgrade was not possible because of the enormous energy loss due to synchrotron radiation. It scales with $\propto E^4/(m_0^4 \cdot r^2)$ where the radius r of the ring accelerator is fixed. Therefore the operation of LEP was stopped in the year 2000, and the accelerator was dismounted in order to give room for the LHC which benefits from the much larger mass of the proton ($(m_p/m_e)^4 \approx 10^{13}$) making much higher energies with the same accelerator radius possible. To achieve higher energies with an $e^+ e^-$ accelerator one has to leave behind the concept of a ring accelerator since its radius would be to large to be realized. Therefore a linear accelerator structure is chosen for the ILC. Figure 1.1 shows a schematic layout of the ILC for a centre-of-mass energy of 500 GeV. The electrons are produced by a photocathode DC gun, while the positrons are produced by an undulator, driven by the 150 GeV main electron beam. It produces high energetic photons directed to a target where they produce a beam of electron-positron pairs. The electrons and remaining photons are separated from the beam and dumped. Two damping rings with a circumference of 6.7 km, operating at a beam energy of 5 GeV, are used to reduce the emittance of the electrons and positrons respectively (i.e. to compress the beam, reduce the transverse and to equal the longitudinal momentum of the electrons and positrons in a bunch). A small emittance beam is needed in order to be accepted by the following beam transport system. It guides the particle beam to the main linear accelerator which utilises 1.3 GHz superconducting radio frequency cavities with an average gradient of 31.5 MV/m to accelerate the electrons and positrons to the final energy of 250 GeV. The high accelerating gradient is crucial in order to keep the size of the accelerator acceptable (the actual design has a total length of 30 km). A beam delivery system finally brings the two beams to collision with a 14 mrad crossing angle at a single interaction point which is planned to be shared by two individual detectors, operated by two independent collaborations.

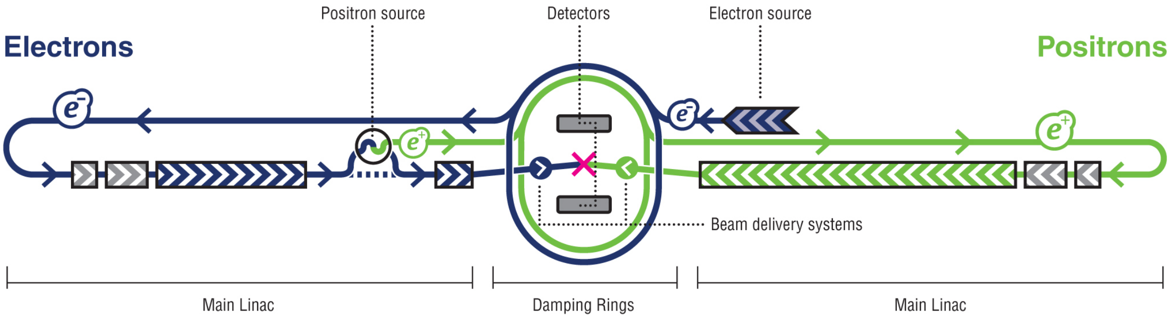

Figure 1.1: A schematic layout of the International Linear Collider. The overall extension is about ≈ 30 km.[1]

Detector Concepts

The detectors for the ILC have to meet the high precision requirements given by a broad physics program since the actual physics case of the ILC depends on the outcomes of the LHC experiments. Four different detector concepts are being studied which represent different approaches and technology choices [1]:

- The Silicon Detector (SiD) Concept[4]
- The Large Detector Concept (LDC)[5]
- The Global Large Detector (GLD)[6]
- Fourth Concept (“4th”) Detector[7]

All have in common an inner vertex detector, a tracking system either based on silicon or a gaseous based *Time Projection Chamber* (TPC), a calorimeter for jet energy measurements and a muon system. In the following the emphasis is placed on the LDC. Figure 1.2 shows a schematic view of the LDC. The main features are a large volume tracking device and highly granular electromagnetic and hadronic calorimeters, all inside of a strong magnetic field of up to 4 Tesla. The design is completed by a muon system covering the complete solid angle outside the coil.

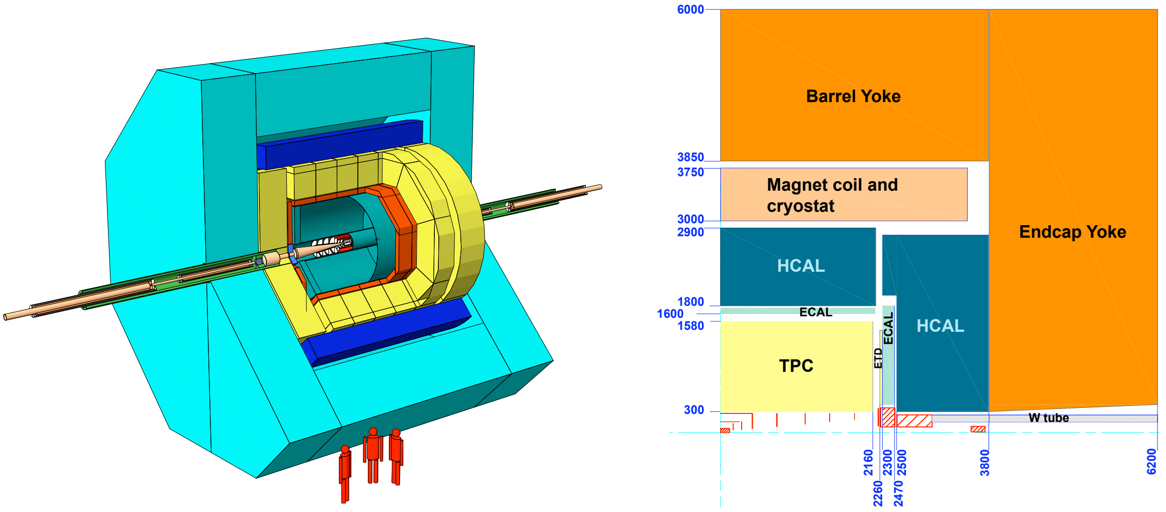

Figure 1.2: Left: Schematic view of the layout for the Large Detector Concept. **Right:** One quarter of the LDC detector with the dimensions in [mm] [1]

The tracking device is used to measure the momenta of charged particles which make up on average 65 % of a jet’s energy. It is designed in a way to minimise the dead material which particles have to traverse before entering the calorimeters. The tracking device is located closest to the interaction point and has several subdetector systems: A high precision five layer pixel vertex detector provides an excellent point resolution giving the full vertex topology of the event. It is followed by a system of silicon strip and pixel detectors used to extend the vertex detector. They also match the particle tracks from the vertex detector with the tracks measured by the large area TPC as the main tracking device. A typical particle jet consists of charged particles, photons and neutral hadrons. The main principle of a new approach for event reconstruction, often referred to as particle flow approach, is to measure the particle energy in a jet with the detector best suited for it: The energy of charged particles is measured with the tracking device and the energy of uncharged particles like photons or neutral hadrons is measured with the calorimeters. Therefore the energy of charged particles deposited in the calorimeters needs to be isolated from the neutral energy in order to avoid double counting. This request motivates the design of the calorimetric system. It consists of a high granular electromagnetic calorimeter (ECAL) which is optimised to measure the energy of photons and electrons and an also high granular hadronic calorimeter (HCAL) (see next sections). The fine segmentation in longitudinal and transversal direction allows to separate the energy deposited by charged and uncharged particles. The calorimeters are surrounded by a large volume superconducting coil, creating a longitudinal B-field of four Tesla. It is surrounded by an instrumented iron return yoke which also serves as a muon detector.

1.2 Calorimeter Physics

In order to measure the energy of a high energetic particle, its property to create a so-called shower of secondary particles when traversing matter is used. During the shower development the initial energy is subdivided into smaller fractions carried by the secondary particles. These (low energetic) particles may then lose energy due to ionisation in a scintillating material producing a visible light signal. Once the remaining energy of an individual particle is too small, the shower process ends and the energy of the remaining particles is absorbed. In general one has to distinguish between two types of particle showers: Electromagnetic showers created by photons, electrons and positrons, and hadronic showers arising from interactions of strongly interacting particles like protons, neutrons and pions. The latter ones are much more complicated to describe due to the large variety of possible interactions.

1.2.1 Electromagnetic Showers

The outline of the following section is as follows: First, a brief overview of the main photon interactions with matter will be given followed by the important interactions of charged particles. Then the electromagnetic shower development will be discussed.

Photon Interactions

Photons are mainly interacting with matter in three ways:

- **Photoelectric effect:** A photon can transfer its total energy to an electron of the material whereas a third object (the nucleus) is needed in order to fulfil energy-momentum conservation of the process. The kinetic energy of the liberated electron is:

$$E_{electron} = E_{photon} - W \tag{1.1}$$

  where W is the energy which is needed to free the electron (also called work function). The probability for photoelectric absorption is higher for more tightly bound electrons.

For x-rays of sufficient energy therefore mainly electrons from the K-shell are affected. The following formula describes the probability τ for photoelectric absorption [8]:

$$\tau \approx \frac{Z^4}{E^3} \tag{1.2}$$

It shows that the interaction is more important for heavy atoms (high atomic number Z) and low energy gamma rays. This equation represents only an approximation since the exponent of Z is varying between 4 and 4.8 for different elements.

- **Compton scattering:** If a photon interacts with a weakly bound electron whereby it only partially transfers its energy, the process is referred to as Compton scattering. The energy of the electron can be calculated with the Compton formula:

  $$E_{electron} = h\nu \left(1 - \frac{1}{1 + \frac{h\nu}{m_0 c^2}(1 - \cos\vartheta)} \right) \tag{1.3}$$

  where ν is the photon frequency, ϑ is the scattering angle of the photon and m_0 is the electron mass. The electron energy for Compton scattering can adopt continuous values until a maximum value for $\vartheta = 180$ is reached, while the energy of photoelectrons is discrete.

- **Pair production:** If the photon energy is higher than two times the rest mass of the electron, an e^+e^- pair can be produced. An electric field is needed either from an electron or from the nucleus in order to fulfil energy-momentum conservation. For high energies, pair production is the dominating process and the photon interaction can be described by the radiation length X_0 defined for electrons and positrons (see Bremsstrahlung):

  $$\lambda_{pair} = \frac{9}{7} X_0$$

  where λ_{pair} is the mean free path of an x-ray for pair production. This means that a high energetic photon will create an e^+e^- pair with a probability of $1 - e^{-7/9} = 54\%$ when passing one radiation length X_0.

In addition to these three interactions there are other processes like photo-nuclear reactions, whereby the photon interacts with a nucleus of the traversed material (e.g. nuclear excitation). These processes only play a secondary role since the contribution to the total energy loss is much smaller and only relevant at high energies. For small energies, elastic scattering of photons with electrons plays a role. It is referred to as Rayleigh scattering. Since there is no energy exchanged it doesn't contribute to the energy loss and only increases the transversal extension of the shower. The cross sections of the various photon interactions in lead are shown in figure 1.3.

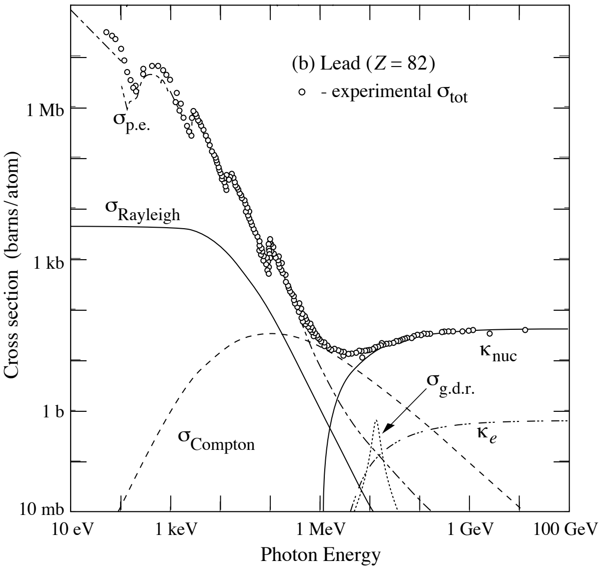

Figure 1.3: Photon cross section per atom as a function of the photon energy for lead. The circles represent measured data.
$\sigma_{p.e.}$ = Photoelectric absorption; $\sigma_{Rayleigh}$ = Rayleigh scattering; $\sigma_{Compton}$ = Compton scattering; κ_{nuc} = Pair production nuclear field; κ_e = Pair production electron field; $\sigma_{g.d.r.}$ = Photonuclear interactions (giant dipole resonance) [9]

Charged Particle Interactions

The main interactions of charged particles are listed in the following:

- **Ionisation and excitation:** Charged particles can interact electromagnetically with the electrons of an atom or molecule and excite or ionise atoms or molecules if their energy is high enough. The excited electron will subsequently return to its ground state by the emission of photons. This process is used in scintillators to produce visible light (see section 4.1).
  Heavy charged particles (e.g. nuclei) lose their energy mostly by ionisation. The mean energy loss dE per unit path length dx is given by the Bethe Bloch formula [10]:

  $$-\left.\frac{dE}{dx}\right|_{Ion} = 4\pi N_A r_e^2 m_e c^2 z^2 \frac{Z}{A}\frac{1}{\beta^2}\left[ln\left(\frac{2m_e c^2\gamma^2\beta^2}{I}\right) - \beta^2 - \frac{\delta}{2}\right] \tag{1.4}$$

  where z is the charge of the ionising particle in terms of the electron charge. Z and A are the mass and the atomic number of the absorber material. The electron mass is denoted m_e and r_e is the classical electron radius. N_A is the Avogadro number, I is the characteristic ionisation constant of the material and δ is a parameter used to describe the partial shielding of the transversal electric field of the relativistic particle. The energy loss due to ionisation therefore only depends on the velocity v ($\beta = v/c$, $\gamma = 1/(1-\beta^2)$), the charge z and on the absorber material properties.

- **Bremsstrahlung:** Fast charged particles can interact with the Coulomb field of the nucleus in the traversed material. Thereby they lose energy in form of electromagnetic radiation. Its contribution to the total energy loss is large for particles with small masses (i.e. electrons and positrons) and high energies. The energy loss due to bremsstrahlung for electrons is given by:

$$-\frac{dE}{dx}\bigg|_{Brems} = \frac{E}{X_0} \tag{1.5}$$

Where X_0 is the so-called radiation length. Integration of equation 1.5 gives:

$$E(x) = E_0 \cdot e^{-x/X_0} \tag{1.6}$$

The radiation length represents the mean distance an electron or positron can travel before it has lost $(1 - 1/e)$ of its initial energy due to bremsstrahlung. It is a function of the material properties [10]:

$$X_0 = \frac{716.4 \cdot A}{Z(Z+1)ln(287/\sqrt{Z})}[g/cm^2] \tag{1.7}$$

Figure 1.4 shows the calculated energy loss, normalised to the material density of a μ^+ in copper as a function the $\beta\gamma$-factor and the momentum. Normalisation to the density provides a value which allows to compare materials with different densities (e.g. gaseous with solid materials). For values of $\beta\gamma$ in the range between 0.1 and 500 the energy loss is well described by the Bethe Bloch formula. For higher values bremsstrahlung has to be taken into account. Figure 1.2.1 shows the schematic development of an electromagnetic shower. A high energetic photon interacts with the material and produces an e^+ e^- pair. These electrons and positrons may radiate bremsstrahlung photons which in turn can produce further e^+e^- pairs. The shower process ends if the energy of the secondary particles reaches the critical energy E_c. It characterises the energy where ionisation effects start to dominate over bremsstrahlung. The definition is as follows:

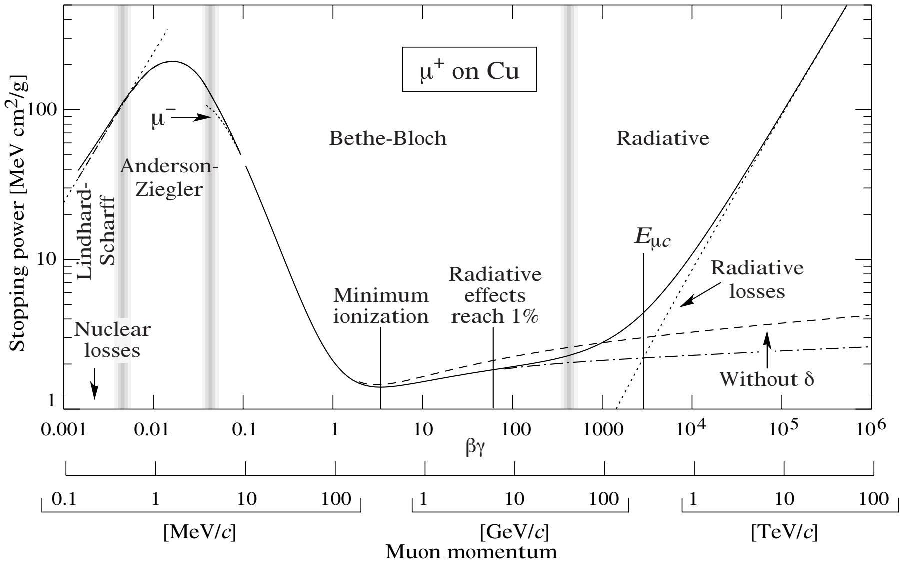

Figure 1.4: Stopping power for positive muons in copper.[9]

$$-\frac{dE}{dx}(E_c)\bigg|_{Brems} = -\frac{dE}{dx}(E_c)\bigg|_{Ion} \tag{1.8}$$

For heavy elements ($Z \geq 13$) it can be approximated by the following formula [10]:

$$E_c = \frac{550\,\mathrm{MeV}}{Z} \tag{1.9}$$

The transverse extension of an electromagnetic shower is given by the Moliére radius which gives half of the radius of the cylinder around the shower axis containing 95% of the shower energy ($E(2R_m) = 0.95 \cdot E_{shower}$). It can be expressed by the radiation length by the following formula:

$$R_m = (21\,\mathrm{MeV} \;\cdot X_0)/E_c \tag{1.10}$$

In applications typically a material with a small Moliére radius is chosen in order to contain the whole shower in a compact device. The tracks from two close particles can be better separated if the transversal shower extension is small.

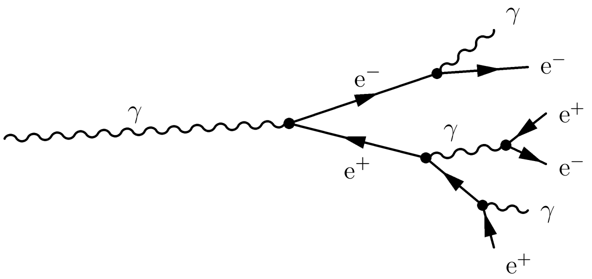

Figure 1.5: Schematic view of an electromagnetic shower. A high energetic photon comes from the left and produces an electron-positron pair which in turn can lose energy via bremsstrahlung giving rise for new photons. If the energy of the photon is high enough, it can produce further electron-positron pairs. Thereby it propagates not only longitudinally but also transverse. If the energy of the subsequent particles is smaller than the critical energy, E_c the shower ends.

1.2.2 Hadronic Showers

A detailed explanation of hadronic showers is more complicated than of electromagnetic showers since hadrons are interacting strongly. A charged hadron (e.g a π^+) may ionise the material before it performs a cascade of nuclear interactions giving rise to a huge variety of secondary particles. Also the absorber nucleus may become excited with subsequent nuclear fission. Electromagnetic interacting hadrons can also initiate an electromagnetic shower which therefore represent a subcomponent of the hadronic shower. However the shower development is mainly based on the strong interaction and can be described statistically for a given material by the nuclear interaction length λ_{int}. The probability for a strong interaction after travelling the distance x is given by the following equation:

$$P_{strong} = 1 - e^{-x/\lambda_{int}} \tag{1.11}$$

The nuclear interaction length is in general larger than the radiation length. For iron the ratio is: $\lambda_{int}/X_0 \approx 9$.

1.2.3 Sampling Calorimeters

Different types of calorimeters exist. They can be homogenous like in the case of lead-glass calorimeters or they can have an inhomogeneous structure made of several materials. A common calorimeter of the latter type is the sampling configuration. It has an alternating structure of layers of absorber material and an active material (e.g. scintillator) used to create a signal. The absorber material is needed to initiate the particle multiplication due to the shower process. For this purpose in common materials with small radiation- and nuclear interaction lengths (high Z, e.g. tungsten, lead, steel) are chosen. The low energetic fraction of the secondary particles may then lose energy due to ionisation in the active layers yielding an amount of scintillation light proportional to the number of particles. The active layers have in general a lower density than the absorber material and weakly influence the shower development. The visible energy (e.g. scintillation light) is in general much smaller than the total energy, especially for the hadronic calorimeter due to the inelastic nuclear interactions of hadrons. However the measured energy E_{vis} is proportional to the total energy. Therefore total energy can be reconstructed for a correct calibration.
The energy resolution is an important characteristic of a calorimeter. It is described by the following formula:

$$\frac{\sigma(E)}{E} = \frac{a}{\sqrt{E}} \oplus \frac{b}{E} \oplus c \tag{1.12}$$

The statistical fluctuation of the number of particles produced in the shower is described by $\sqrt{N}$ (Poisson distributed). Since the energy is proportional to the number of slow particles $E \propto N$, it follows the so-called "sampling term" $a/\sqrt{E}$ of the energy resolution. Another factor influencing the energy resolution is caused by noise fluctuations due to instrumental effects like electronics noise. The relative noise scales with the energy like $\sigma_{Noise}(E)/E \propto 1/E$. The third term contributing to the energy resolution is the is the so-called constant term c. It contains contributions from calibration errors, non-uniformities and non-linearities of the detectors. It is the limiting factor at high energies.

1.3 The Calorimeter Prototype

Within the CALICE collaboration several different calorimeter designs are studied. For the hadronic calorimeter there are two concepts: A digital version with a small cell size of 1×1 cm^2 where each cell provides only digital (yes or no) information. The more classical concept is the analogue hadronic calorimeter (AHCAL) with bigger cell size and information about the amount of energy deposited in each calorimeter cell. To study the concept of a high granular calorimeter with individual cell readout a 1 m^3 "physics prototype" for the analogue hadronic calorimeter has been built at DESY in Hamburg. At this point the emphasis of the design is dedicated to the physics performance of such a calorimeter. Simulation models have to be found which predict the appearing physics, allowing to optimise the design. The next step will be a technical prototype considering the technical specifications which have to be met for the final design of the whole detector (i.e. mechanical structure, power consumption, cooling and readout) [11].
The "physics prototype" has a steel-scintillator sandwich structure with small scintillating tiles of 0.5 cm thickness in the size ranging from $3 \times 3\,\mathrm{cm}^2$ to $12 \times 12\,\mathrm{cm}^2$. Figure 1.6 shows

on the left side a photograph of one layer of scintillating tiles. The complete prototype consists of 38 of these layers alternating with 1.6 cm thick steel absorber plates and is shown in figure 1.8. It was exposed to electron and hadron beams at test-beam areas of DESY and CERN. The thickness of the prototype corresponds to a total nuclear interaction length of $4.5\,\lambda_{int}$. On the right side of figure 1.6 a photograph of a single $3 \times 3\,\mathrm{cm}^2$ tile is shown. The tiles consist of an organic scintillator, having the advantage of a fast decay time and being produceable in principally every shape compared to inorganic scintillators (section 4.1) which are often used to detect gamma rays. The tiles are chemically treated (matted) on the lateral surfaces, and the up- and down-sides are covered with a highgly reflective foil to inhibit the escape of scintillation light. If a particle crosses the tile, it produces a certain amount of blue scintillation light depending on the energy and type of the particle (≈ 5000 photons per *minimum ionising particle* (MIP) see figure 1.4). The light, produced at different positions in the tile, is collected with a $1\,mm$ diameter wavelength-shifting fibre (WLSF) which is placed in a 2 mm deep groove on the scintillating tile. It absorbs the blue scintillation light and emits green light (see figure 1.7) since the light detector has the highest detection efficiency for green light. One end of the WLSF is covered with highly reflective foil while the other end is guided to the small $1 \times 1\ \mathrm{mm}^2$ active surface of a novel kind of photon detector, the so-called silicon photomultiplier (SiPM). Also other photon detectors like avalanche photodiodes and photomultipliers were studied ([13] and [14]) for the scintillation light readout, but finally the SiPM was chosen to built the $1\mathrm{m}^3$ prototype. It is well suited for this application due to the high gain (comparable to vacuum photomultipliers), the small size which allows a direct light readout at the tile, and the insensitivity to magnetic fields. Since the calorimeter will be placed inside the magnetic field in the final design, this is an important feature. The SiPM was developed at the *Moscow Engineering Physics Institute* (MEPhI). Nowadays there are several manufacturers on the market producing similar devices. Recently another device, the so-called multi-pixel photon counter (MPPC) from the company HAMAMATSU, became available and was tested as a potential candidate for the tile readout [15]. Due to its high

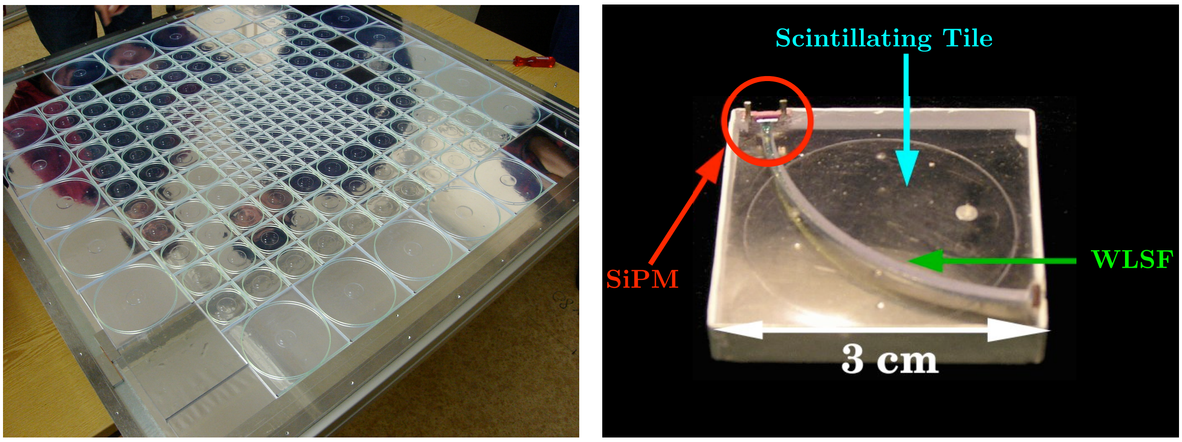

Figure 1.6: Left: One layer of scintillating tiles for the analogue HCAL. The tile sizes ranges from $3 \times 3 \times 0,5\ \mathrm{cm}^3$ in the middle to $12 \times 12 \times 0,5\ \mathrm{cm}^3$ in the outer region. **Right:** Scintillating tile with wavelength-shifting fibre and readout via SiPM. The edges of the scintillating tile were chemically treated to produce small reflective bubbles on the surface. Inside of the calorimeter the up- and down-side will be covered with reflector foil [12].

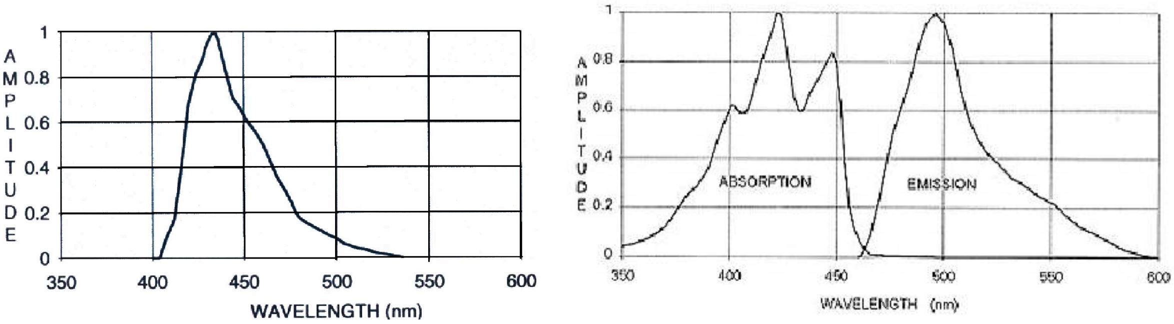

Figure 1.7: Left: Emission spectrum of the scintillator used. **Right:** Absorption and emission spectrum of the wavelength shifting fibre.

sensitivity in the blue region, readout without a WLSF may become possible representing a more elegant solution, easier extendable for the large scale future design.

Since the variety of available devices is growing (there are already several producers on the market), it is necessary to characterise the devices, which means to determine the basic parameters describing the performance, in order to allow the selection of a specific device.

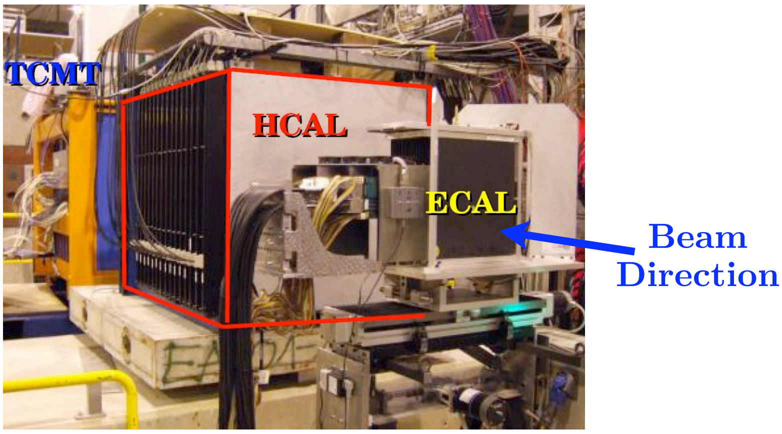

Figure 1.8: Photograph of the hadronic calorimeter prototype (HCAL) together with the electromagnetic calorimeter prototype (ECAL) and the tail catcher and muon tagger system (TCMT). All three prototypes were operated together at the test beam areas of DESY and CERN [12].

Chapter 2

Light Detectors

Many different types of radiation detectors have been developed to fit the special needs that arise with a certain application field. A recent candidate of these devices is the *Silicon Photomultiplier* (SiPM)[1] or *Multi Pixel Geiger Mode Avalanche Photodiode* (MPGAPD) which was recently developed [16, 17] and has become commercially available lately. The following chapter will provide a brief overview of the different kinds of light detectors. For a detailed review, the reader is referred to the standard literature [18, 19].

2.1 Photomultipliers

A very common kind of photodetector is the vacuum *Photomultiplier Tube* (PMT). It was developed already in the nineteen-thirties [20], but still plays a dominant role in many fields of application. The main structure has not changed a lot since the beginning and is shown in figure 2.1. The operation principle is based on the multiplication of free electrons produced via the photoelectric effect on the photocathode (usually a thin layer of alkali metals with a very low work function W (see equation 1.1). The electrons emitted into the vacuum are focused and accelerated by a focusing electrode towards the first dynode. When they hit the first dynode, secondary electrons are produced with a multiplication factor of $n \approx 3 - 10$. The dynodes are arranged in the way that the secondary electrons are focused to the next dynode and so forth, and finally the electrons are collected at the anode. The number of electrons resulting from a single photoelectron emitted from the photocathode is referred to

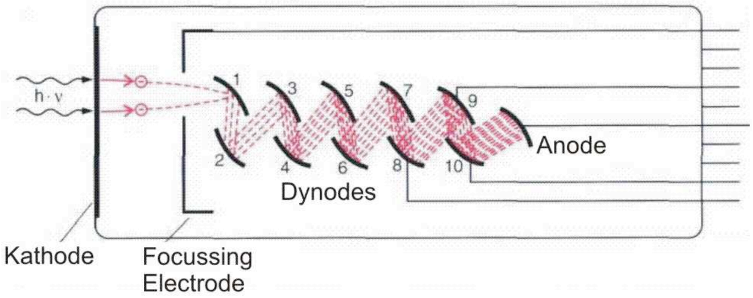

Figure 2.1: Schematic view of a linear focussed photomultiplier tube

---

[1] There are many different names in use for the same device (E. g. *Multi Pixel Photon Counter* (MPPC) from HAMAMATSU, *Silicon Photomultiplier* (SPM) from SensL, *Multi-pixel Avalanche Photodiode* (MAPD) from Voxtel, *Solid State Photomultiplier* (SSPM) from Photonique). In this thesis the abbreviation SiPM was used as a general name, if the producing company is not emphasised explicitly.

as the gain M of the photomultiplier and can be understood as an intrinsic amplification of the primary current from the cathode produced by photon absorption. Typical values are in the range of $M \approx n^d \approx 10^6$ while d is the number of dynodes. A high gain is crucial for the detection of single photons in order to achieve a good *Signal to Noise Ratio* (SNR).
The disadvantages of PMT's are that most of them are bulky in shape and fragile due to the needed vacuum-tube structure. The high voltage (typical 2 kV) needed to operate a PMT is difficult to handle. In addition the electrostatic focusing inside the tube is disturbed by an external magnetic field making the operation under such ambient conditions difficult. For applications where these drawbacks cannot be accepted, different kinds of photodetectors have to be used relying on different physical mechanisms.

2.2 Semiconductor Detectors

The disadvantages of PMT's can partially be overcome by semiconductor detectors. This section gives an overview of the family of these detectors and their working principles.

Material Properties

Materials in general can be categorised in three main families, depending on their conductivity which is strongly related to the energy-band structure (see figure 2.2):

- **Insulators:** The energy gap between the valence and the conduction band is large. The valence band is fully occupied and therefore the charge carriers cannot move, resulting in a high resistivity.
- **Semiconductors:** At low temperatures the situation is similar to insulators: The valence band is completely filled and the conduction band is empty, but at room temperature electrons can be thermally excited into the conduction band due to the small band gap.
- **Conductors:** The conduction and the valence band can be overlapping, or the conduction band is partially filled. If this is the case, the material shows a high conductivity.

Electron-Hole-Pair Production

If a photon transfers its energy to an electron by photoelectric absorption or Compton scattering, it can lift the electron from the valence to the conduction band. Thereby a free electron and hole are produced in the conduction and valence band, respectively. This process is schematically shown in figure 2.3 for photons of different energies. If the photon energy is higher than the band gap the electron will be lifted to an empty state in the conduction band and subsequently move towards the edge of the band gap (intraband transition) by non-radiative lattice interactions or emission of low energetic photons. If the photon energy is lower than the band gap, generation of a charge carrier is possible if intermediate states are available due to lattice impurities. In the shown process (right side of figure 2.3) a hole is produced in the valence band together with the ionisation of a local state caused by an impurity (illustrated as a blue square). Semiconductor materials in general show unavoidable impurities due to the production process, but often impurities are added on purpose in a process

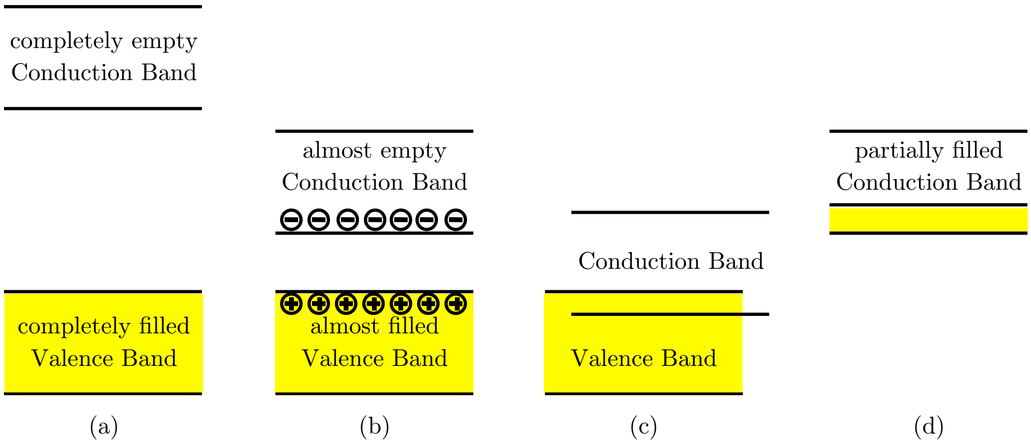

Figure 2.2: Band structure of a) insulator, b) semiconductor, c) and d) conductor. The vertical direction represents the energy.

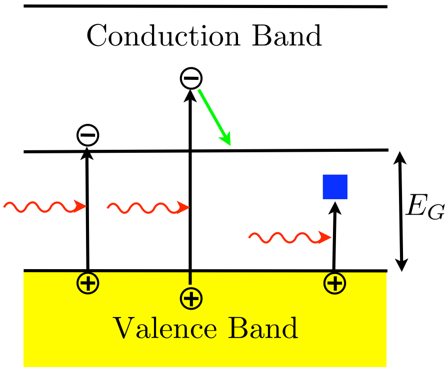

Figure 2.3: Electron-hole production by absorption of photons with different energies. From left: $E_{ph} = E_G$, $E_{ph} > E_G$ and $E_{ph} < E_G$. The blue box represents a state caused by impurities in the material.

called doping of a semiconductor to generate the desired properties. By adding atoms with five possible covalent bonds (arsenic) to a lattice of atoms which undergo four bonds (silicon), the fifth electron is only weakly bound and can be excited easily to the conduction band. In the energy band model this is equivalent to additional states close to the bottom edge of the conduction band (see figure 2.4). By adding atoms with only three valence electrons (boron) to the silicon lattice, one of the four covalent bonds is only occupied by one electron instead of two electrons like in the other three bonds. These states can trap electrons and show a smaller binding energy for the electron than the other three bonds. Therefore the energy level of these states is slightly higher then the upper edge of the valence band. The first type is referred to as n-doped while the second type is referred to as p-doped material. The generated electrons and holes will not exist for a infinite time. They recombine through phonon excitation and under emission of photons. The actual lifetime of a carrier strongly depends on the specific type and size of the band gap. In general one distinguishes between direct and indirect band gaps where for the latter one a direct transition is suppressed due to the different momentum values of the states showing the smallest energy difference. The shape of the energy bands for silicon and gallium-arsenide are shown in figure 2.5. Recombination occurs in silicon via intermediate states caused by impurities.

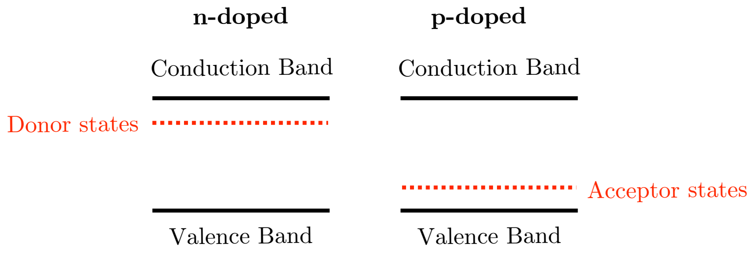

Figure 2.4: Schematic view of the band structure of extrinsic semiconductors. The energy gap between the donor states and the conduction band is small $\approx 0.05\,\mathrm{eV}$ [19]. Therefore these states will be almost completely ionised at room temperature yielding free electrons in the conduction band. The acceptor states are close to the valence band. Therefor electrons can be easily excited from the valence to the acceptor states yielding free holes in the valence band.

2.2.1 p-n-junctions

By putting a p- and an n-doped material together, a strong gradient of charge carrier concentration at the contact surface is generated. This causes a diffusion current of electrons to the p-side and holes to the n-side, respectively, where they recombine. A thin layer of negligible small charge carrier concentration, the so-called depletion layer is formed. At the same time an electric field is generated due to the increased negative charge in the p-region and positive charge in the n-region which forces an opposite current to the drift current. A stationary equilibrium is found if the sum of both currents equals zero.

If a reverse bias voltage $U_{bias} < 0$ is applied to the p-n diode, the depletion width is increasing and can be described with the following equation [19]:

$$d = \sqrt{\frac{2\epsilon\epsilon_0(N_A + N_D)(U_{bi} - U_{bias})}{q_e N_A N_D}} \approx \sqrt{\frac{2\epsilon\epsilon_0(U_{bi} - U_{bias})}{q_e N_A}} \quad \text{, for } N_D \gg N_A \qquad (2.1)$$

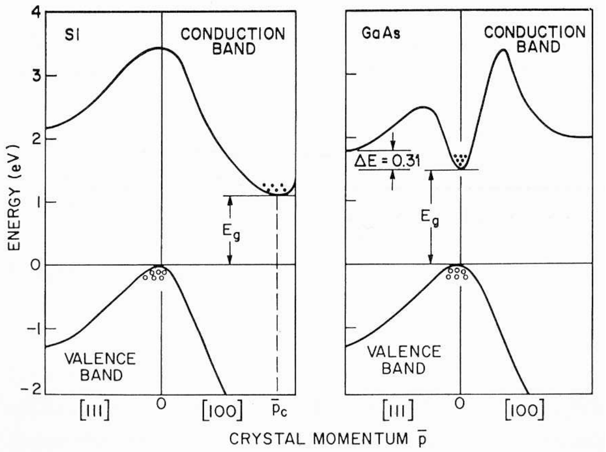

Figure 2.5: Band structure for silicon (left) and gallium-arsenide (right). The x-axis represents the momentum in a direction of the crystal described by the Miller indices. [19]

where ϵ and ϵ_0 are the dielectric constant and the permittivity "in vacuo", respectively. U_{bi} is the so-called built in voltage caused by the electric field due to the different doping concentrations N_A and N_D of the n- and p-layer. q_e is the elementary charge. One can see that the depletion region increases with increasing reverse bias voltage.
The depletion region exhibits a capacitance which can be calculated using (2.1), and again assuming a strong asymmetric doping profile ($N_D \gg N_A$) [19, 18]:

$$C_D = \frac{\epsilon\epsilon_0 A}{d} = \sqrt{\frac{\epsilon\epsilon_0 q_e N_A}{2(U_{bi} - U_{bias})}}A\,, \tag{2.2}$$

where A is the diode surface. The diode capacitance will decrease with increasing reverse bias voltage until a minimum value is reached. This is the case if the depletion region reaches the back of the semiconductor material at the so-called reach-through voltage.
If a p-n-junction is illuminated with light, electron-hole pairs can be generated by photon absorption. Due to the high electric field present, electrons and holes will rapidly drift into the n- and p-region, respectively, with low probability for recombination (see figure 2.6). This will generate a current which is proportional to the photon flux. If the electron-hole pair is generated outside of the high-field region, the probability for recombination is higher and the

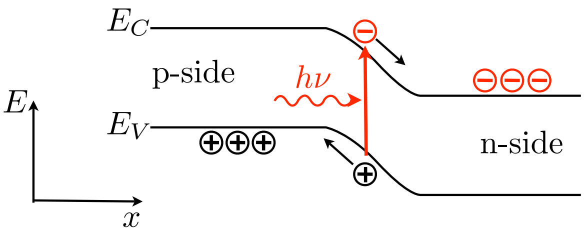

Figure 2.6: A photon creates an electron-hole pair by lifting an electron from the valence to the conduction band. E_C and E_V are the lower and the upper edge of the conduction and valence band, respectively.

efficiency is reduced (i.e. no photocurrent is generated). The absorption depth of photons and therefore the charge collection efficiency varies with the wavelength. The radiation intensity $P(s)$ at the depth s is described by the following formula:

$$P(s) = P_0 \cdot (1 - R) \cdot e^{-\alpha(\lambda)s}\,, \tag{2.3}$$

where P_0 is the initial light intensity. One part of the light is reflected at the surface which is described by the factor $(1-R)$. The remaining light is absorbed at a certain depth, depending on the attenuation coefficient $\alpha(\lambda)$. The attenuation coefficient for different semiconductor materials is shown in figure 2.7. In particular blue light ($\lambda = 400nm$) will only penetrate roughly one micrometer in silicon due to the high attenuation coefficient. To optimise the detection for short wavelength photons (blue light), the covering layers showing a reduced or even no efficiency have to be as thin as possible. To explain the properties of a real photodiode it is helpful to define an equivalent circuit made of ideal components; this is shown in figure 2.8. It is given by a parallel circuit consisting of a current source I_{ph}, an ideal diode D_{id} which allows current only to flow into the forward direction, a capacitor C_{diode} and the so-called shunt resistor R_{sh}. A series resistor R_S refers to the finite resistance of the metal leads and the metal silicon contacts.

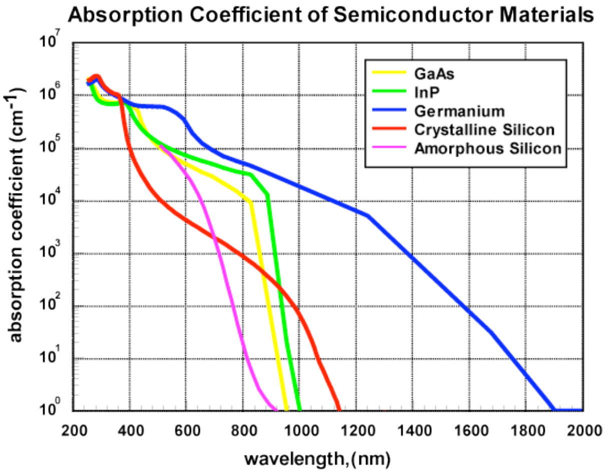

Figure 2.7: Optical attenuation coefficients for different semiconductor materials. $1/\alpha$ is the depth where the light intensity is reduced to $1/e$ of the initial value [21].

2.2.2 PIN-Photodiodes

Following equation 2.3 the depletion layer should be large enough to absorb photons with longer wavelengths. Often an additional intrinsic layer is added between the p- and n-layer (PIN-photodiode), and the device is used under moderate reverse bias voltage. In this way the depletion region is extended over the complete intrinsic layer resulting in higher detection efficiency. Another positive effect of an additional intrinsic layer is the reduced diode capacitance C_D because of the relation (see equation 2.2):

$$C_D = \frac{\epsilon\epsilon_0 A}{d} \approx \frac{\epsilon\epsilon_0 A}{x_i} \tag{2.4}$$

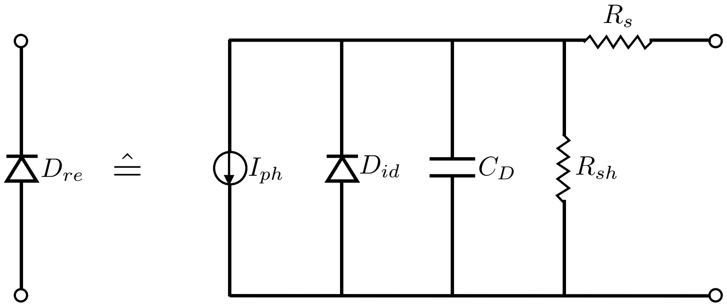

Figure 2.8: The equivalent circuit of a real photodiode D_{re} is a parallel circuit consisting of a current source I_{ph}, an ideal diode D_{id} which allows current only to flow into the forward direction, a capacitor C_D and the so-called shunt resistor R_{sh}. There is also a series resistor R_S referring to the finite resistance of the metal leads and the metal silicon contacts.

where x_i is the thickness of the intrinsic layer. A smaller capacitance results in a higher cut-off frequency which is defined as the frequency where the output for a sine-wave modulated light signal decreases by 3 dB compared to the output at 100 kHz [22, 23]. It can be described by the following equation:

$$f_c = \frac{1}{2\pi \cdot C_D \cdot R_L}$$

where R_L is the load resistance. On the other hand the depletion width shouldn't be too large since the transit time of the carrier in the depletion region will increase the cut-off frequency. PIN-diodes or photodiodes in general have no intrinsic charge amplification making their performance stable under temperature fluctuations. Therefore they are well suited for calibration or monitoring purposes. However, due to the missing gain they are not suitable for single photon detection because of the poor signal to noise ratio.

2.2.3 Avalanche Photodiodes

Avalanche Photodiodes (APD's) have in principal the same structure as pn- or PIN-diodes. The main difference lies in the applied bias voltage. Due to the high reverse bias voltage a generated electron can produce more, secondary electron-hole pairs by the so-called process of impact ionisation: If the bias voltage is high enough the charge carriers can gain enough energy from the electric field in-between two interactions to excite an electron from the bound state to the conduction band. An important parameter thereby is the impact ionisation coefficient α (not the attenuation coefficient). It is given in units of inverse length and can be interpreted as the number of secondary charge carriers generated while moving by one unit length. It increases exponentially with the electric field and decreases with an increasing band gap E_G. Figure 2.9 shows the impact ionisation coefficients as a function of the electrical field. The ionisation coefficient for electrons in silicon is much larger than for holes. Under moderate bias voltages therefore mainly electrons contribute to avalanche multiplication. Figure 2.10 shows the multiplication of carriers by impact ionisation under the assumption that only electrons contribute to the avalanche process ($\alpha_e/\alpha_h \gg 1$).

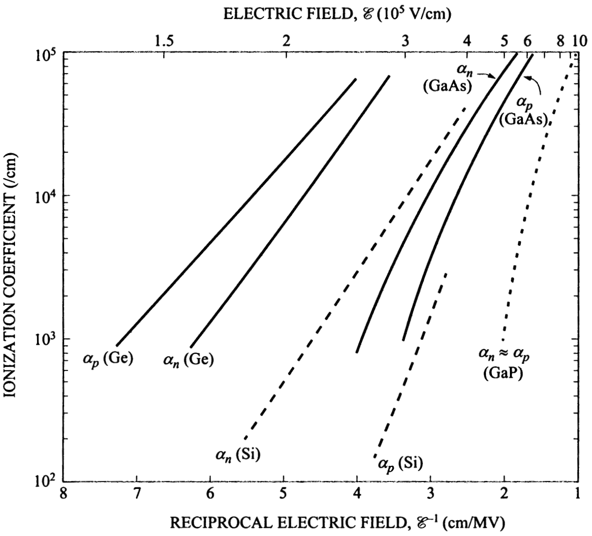

Figure 2.9: Ionisation coefficients for electrons and holes for different semiconductor materials [18].

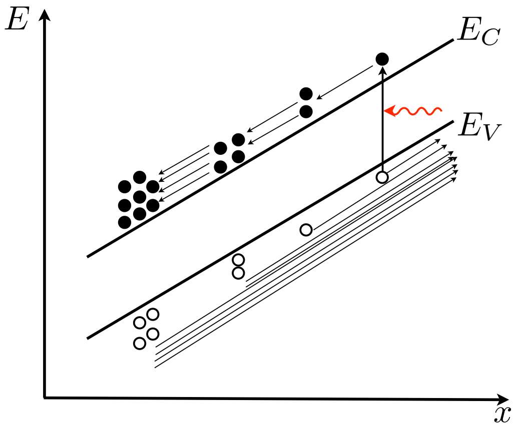

Figure 2.10: Schematic view of the charge carrier multiplication process. An electron-hole pair is generated by photoelectric absorption. The electron and hole are accelerated under the influence of the strong electric field into opposite directions. Electrons can generate electron-hole pairs by impact ionisation whereas the produced holes drift out of the high-field region without amplification. Therefore the avalanche propagates only in one direction and is limited by the length of the high-field region. The resulting current is proportional to the number of primary (photon generated) charge carriers.

The charge multiplication factor M_e can be calculated with the following formula [18]:

$$M_e = \frac{1}{1 - \int_0^L \alpha_h \exp(-\int_x^L (\alpha_e - \alpha_h) dx') dx} \tag{2.5}$$

Where L is the length of the multiplication region. The formula for the multiplication factor of holes M_h is similar to (2.5). If one of the charge carriers dominates the multiplication process, formula 2.5 becomes:

$$M_e = \exp \int_0^L \alpha_e dx \quad , \quad \alpha_e >> \alpha_h \tag{2.6}$$

In this case the gain remains finite and the process is referred to as (linear) avalanche multiplication. Gain values of typically a few hundred can be obtained. The measured current is straight proportional to the initial photon-induced current with the gain M as the proportionality factor:

$$I_{meas} = M \cdot I_{ph}$$

The situation changes if both carrier types contribute to the multiplication process. In the special case of equal ionisation coefficients for electrons and holes, formula 2.5 becomes:

$$M = \frac{1}{1 - \int_0^L \alpha dx} \quad , \quad \alpha_e = \alpha_h = \alpha \tag{2.7}$$

If the reverse voltage across the junction is increased above a certain value which is referred to as the breakdown-voltage U_{break}, the charge multiplication becomes infinite. This process is referred to as avalanche breakdown. From equation 2.7 and 2.5 one can see that this is the case if the denominator becomes zero. Therefore feedback from both carriers types (electrons and holes) is needed, i.e. both carrier types need to perform impact ionisation. This becomes intuitively clear by looking again at figure 2.10: If holes can also create electron-hole pairs the avalanche process is no longer restricted by the size of the multiplication region; the avalanche will propagate in both directions and extend to the whole high-field region.

Avalanche breakdown will therefore yield a growing current through the device. Since the diode itself exhibits a series resistance R_S due to the finite resistance of the metal leads and the metal-silicon contacts (see also figure 2.8), the voltage drop at the p-n-junction will decrease following the equation:

$$U_{junction} = U_{bias} - R_S \cdot I$$

Where R_S is the diode series resistance and I is the current through the device. This results in a finite steady state of the breakdown current, i.e. a positive fluctuation of the breakdown current will reduce the voltage drop at the junction and the current will become smaller. A charge carrier in the depletion layer will therefore result in a very large and stable breakdown current, and subsequent photons cannot be detected unless the breakdown has been stopped. Thus, in order to "reset" the APD for further photon detection, the avalanche process has to be shut-off. This process is referred to as quenching of the device. Two different quenching mechanism are common. In the case of active quenching, avalanche breakdown is detected by measuring the rising current and the circuit is manually opened. Another very convenient way to quench the breakdown is to connect the diode to the power supply through a sufficiently large series resistor $R_q \gg R_{sh}$ where R_{sh} is the shunt resistor of the diode. Typical values for R_q are a few hundred kΩ to a few MΩ. It acts like a virtually open circuit during discharge (time scale of discharge: $R_{sh}C_D$) and causes the diode to recharge slowly with the time scale R_qC_D. An idealised current-voltage-characteristic of this process is shown in figure 2.11. Let's suppose a diode is biased above the breakdown-voltage. As long as no charge carrier is generated (e.g. by photoelectric absorption) the device remains in this state (point **A**). A photon initiates the discharge of the device resulting in a large current which has to be quenched (Point **B**). This is done by the large resistor in series causing the voltage drop to decrease which is indicated as the blue arrow yielding to point **C**. Finally the device is slowly recharged through the large resistor indicated by the green arrow until the starting point **A** is reached again being ready for another discharge. This process is referred to as limited Geiger mode. A high gain can be achieved if the device is used in the Geiger mode since one single photon causes the avalanche breakdown of the whole device. In the 1960's it was realised that avalanche breakdown in pn-junctions can be used to detect single photons [24] needed for photon counting measurements.

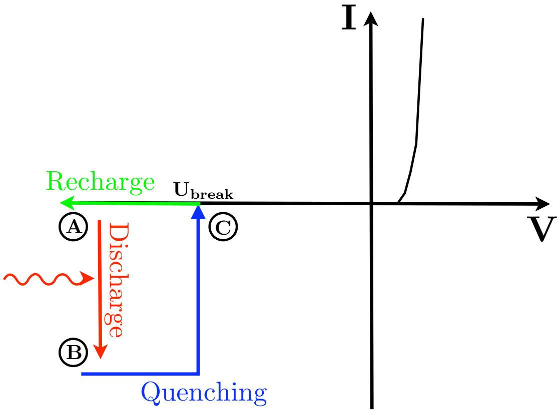

Figure 2.11: Idealised I-V characteristic of an avalanche photodiode operated in Geiger mode.

2.3 The Silicon Photomultiplier (SiPM)

The dynamical range of a photodiode operated in Geiger-mode is strictly limited since it needs time to recover after a photon has been detected. The SiPM shows the high gain of a GAPD, while the dynamical range is increased by putting many GAPD's to a small surface and connect all to a common output. However this yields non-sensitive areas on the device since the individual GAPD's or "pixels" need to be isolated from each other (see section 2.3.2 for more details).

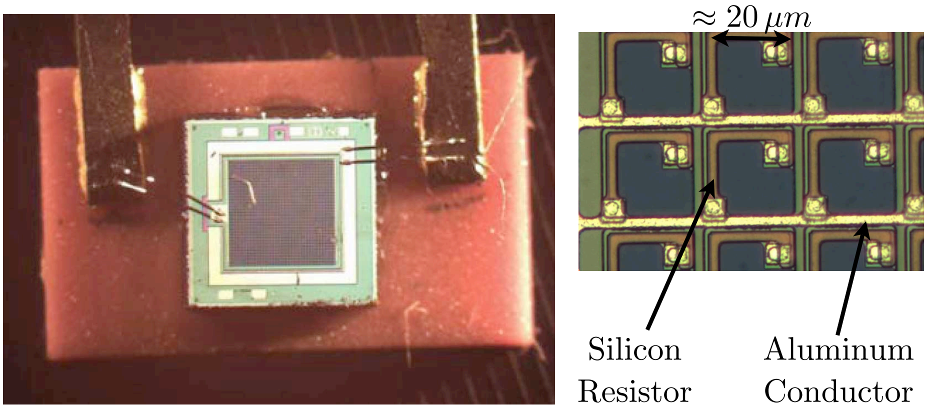

Figure 2.12: Left: Picture of a SiPM produced by MEPHI-PULSAR with the package used for the hadronic calorimeter prototype readout. The active surface is $1 \times 1\,\mathrm{mm}^2$. **Right:** Microscopic picture of the single pixels. The individual silicon resistors and the aluminium conductors connecting all pixels are visible [12].

Layout

A SiPM consists of an array of typically 1000 individual pixels per mm^2. Figure 2.12 shows a picture of a SiPM produced by MEPHI[2]-PULSAR[3] as it is used for the analogue hadronic calorimeter readout. It has a surface area of $1 \times 1\,\mathrm{mm}^2$ and is equipped with $34 \times 34 = 1156$ pixels (right side of figure 2.12).
Figure 2.13 shows the topology of the SiPM. A drift region is formed by a few micrometer thick layer of p^--doped material on the low resistive p^+-type substrate (the $^+$ and $^-$ indicates a high or low doping level respectively). The electric field in this region is not high enough for impact ionisation (see right side of figure 2.13). An electron produced in this region will drift into the thin high-field (typical value $10^5\,\mathrm{V/cm}$) region between the n^+ and the p^+ region where it can trigger an avalanche breakdown if the device is biased over the breakdown-voltage. The avalanche breakdown will be quenched by the built-in silicon resistor on the surface. The guard rings, made of n^--doped silicon, are needed in order to reduce the electric field at the edges of the pixel since impurity levels are higher close to the surface and can lead to unwanted avalanche breakdown and therefore high dark currents. The top of

---

[2] Moscow Engineering and Physics Institute

[3] Pulsar Enterprise, Moscow

the device is covered with an anti-reflecting SIO_2 layer for protection purposes. Aluminium tracks on the surface connect all pixels to the common bias voltage.

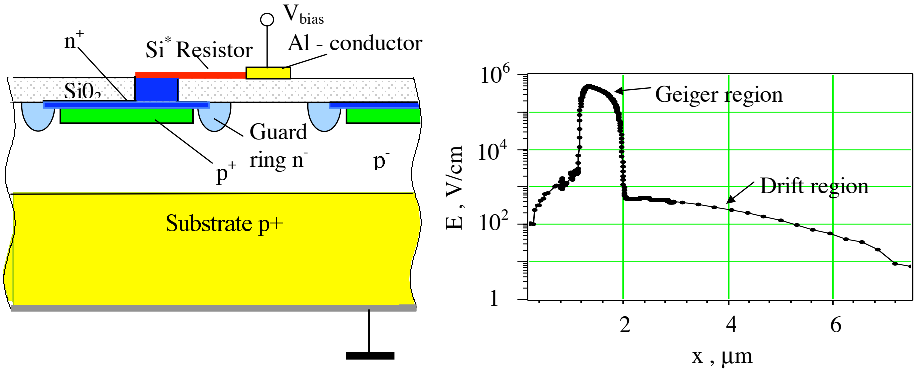

Figure 2.13: Left: Schematic view of the SiPM topology: A few micrometer thick layer of p^--doped material on the low resistive substrate serves as a drift region (see also right side of the picture). An electron generated in this region will subsequently drift into the region between the n^+ and the p^+ layer where the electrical field is high enough for avalanche breakdown. The guard rings reduce the electrical field in order to avoid unwanted avalanche breakdown close to the surface where accidental impurity levels are higher. **Right:** Diagram of the electric field profile in a SiPM [17].

2.3.1 Gain and Single Pixel Response

Since every microcell of the SiPM is operated above the breakdown-voltage, high gain in the range of typically $10^5 - 10^6$ can be obtained which is comparable to the value obtained with a vacuum PMT. The behaviour of a SiPM pixel can be explained by a circuit model which is shown in the following figure:

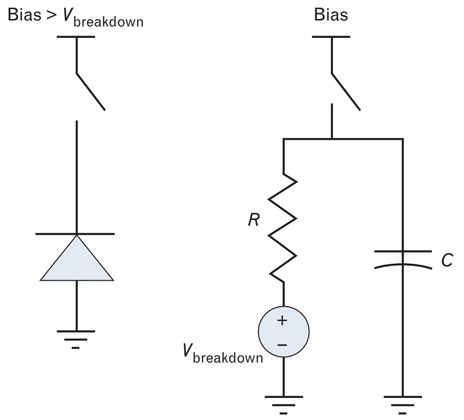

Figure 2.14: Passive-quenching circuits: **Left:** The APD is charged up to some voltage $U_{bias} > U_{break}$ and left open. **Right:** During breakdown the APD behaves like a simple circuit model: A voltage source in series with a resistor and and a capacitor [25].

One has to separate between two possible states of the pixel. The left side shows the pixel in the so-called detection mode. It represents the situation that the diode was biased up to a voltage which is larger than the breakdown-voltage ($U_{bias} > U_{break}$) and the circuit was opened subsequently. The diode will remain in this state until a charge carrier is generated either by photon absorption or by thermal or tunnel excitation (see section 2.3.4) which can trigger avalanche breakdown. The equivalent circuit describing the situation is shown on the right side of figure 2.14. It can be deduced from the equivalent photodiode circuit shown in figure 2.8 by substituting the current source I_{ph} and the shunt resistor R_{sh} in parallel, with a voltage source and a resistor R in series. The diode capacitance C_D is represented in case of the SiPM by C_{pixel}. Applying this simple model the charge flowing out of the capacitor during discharge can be calculated using the formula $Q = C \cdot U$ as follows:

$$Q(t) = C_{pixel} \cdot (U_{bias} - U_{break})(1 - e^{\frac{-t}{R \cdot C_{pixel}}}) \tag{2.8}$$

The gain M can be calculated as follows:

$$\frac{Q(t \to \infty)}{q_e} = N_e = M = \frac{C_{pixel}}{q_e} \cdot (U_{bias} - U_{break}) = \frac{C_{pixel}}{q_e} \cdot U_{over} \tag{2.9}$$

One can see that the gain depends only on the applied over-voltage $U_{over} = U_{bias} - U_{break}$ and the pixel capacitance C_{pixel}. The pixel capacitance (typical value $\approx 20 - 300\,\text{fF}$) shouldn't be too large since the gain will then be very sensitive to voltage fluctuations, introducing noise. The bias voltage should be as stable as possible to reduce gain fluctuations. This model does not take into account the recombination of charge carriers. However it represents a good approximation as we will see in chapter 3.1.

2.3.2 Photon Detection Efficiency

There are many different conventions for the definition of the Photon Detection Efficiency (PDE). In this thesis the following convention was used: The PDE is the ratio of the number of photons recognised by the detector (i.e. number of photoelectrons) over the number of photons arriving at the detector surface. It can be expressed with the following equation:

$$PDE = (1 - R) \cdot \epsilon_{geo} \cdot \epsilon_{avalanche} \cdot QE \tag{2.10}$$

The factor $(1 - R)$ describes the fraction of light which permeates the covering layer. The SiPM has aluminium tracks and built in resistors on its surface (see figure 2.12). Therefore not the whole detector surface is photon-sensitive and the geometrical efficiency has to be taken into account. It is given as the fraction of the active surface to the total surface of the device $\epsilon_{geo} = A_{active}/A_{total}$. By building SiPMs with less, but larger pixels, the ratio can be improved resulting in a higher PDE. However the dynamical range will be smaller, therefore optimisation between dynamical range and PDE has to be done. The factor $\epsilon_{avalanche}$ describes the probability that a produced charge carrier initiates avalanche breakdown. It depends on the applied bias voltage and on the location of the carrier production. For example an electron produced close to the n$^+$-layer (for a n over p configuration like in figure 2.13) has a smaller probability to initiate a Geiger-discharge compared to an electron produced at the centre of the p$^+$-layer [26]. Finally, the factor QE gives the probability for the production of an electron-hole pair. It depends on the photon wavelength and on the width of the active layer (depletion region). Using equation 2.3 one can obtain a formula for the quantum efficiency:

$$QE \approx (1 - e^{-\alpha \cdot d})$$

where α is the absorption coefficient which strongly depends on the wavelength. $1/\alpha$ gives the mean distance a photon can travel before it is absorbed. Since this number is very small for photons with short wavelength (400 nm: $1/\alpha < 1\,\mu$m) the sensitivity is limited by the minimum thickness of the covering layers. For photons with long wavelengths there is an energy cut-off since the photon energy becomes too small to bridge the energy gap between the valence and the conduction band (silicon ≈ 1.1 eV). The traditional SiPMs are optimised for green light, while the *Multi Pixel Photon Counter* (MPPC) from the company HAMAMATSU shows a maximum sensitivity in the blue wavelength region.

2.3.3 Dynamical Range

Each pixel works as an APD operated a few volts higher than the breakdown-voltage in limited (non linear) Geiger mode (GAPD). This means, if a photon is absorbed it produces a large output current which is stopped by the passive quenching mechanism. If two photons hit one microcell at the same time the resulting output signal will be the same as in the case of one photon. The key feature of the SiPM is that many pixels are placed on a small area (typically $100 - 1600/\text{mm}^2$). The output of all pixels is set to a common load so that the resulting output signal is the sum of the individual pixel signals.

$$Q_{Signal} = N_{fire} \cdot Q_{pixel}$$

where N_{fire} is the number of firing pixels and Q_{pixel} is the charge laid off at the Geiger-discharge of a single pixel ($Q_{pixel} = M \cdot q_e$). This working principle is schematically described in figure 2.15. Each microcell represents a GAPD with its own quenching resistor in series.

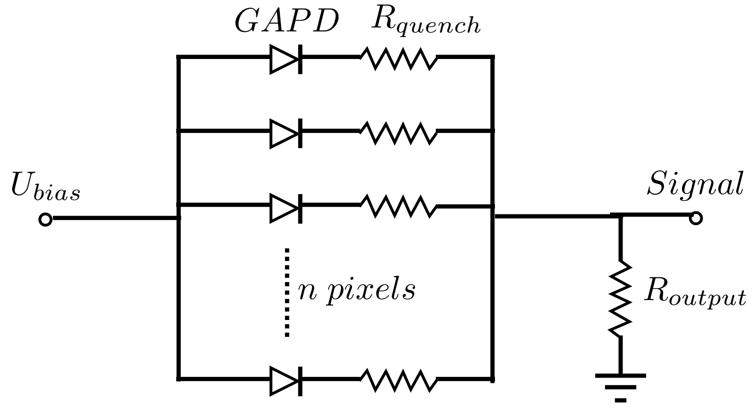

Figure 2.15: Schematic illustration of the SiPM. Each pixel corresponds to a APD operated in Geiger mode with an individual quenching resistor. The output of all pixels is connected to a common load, and therefore the output of the device is a sum of all pixel signals.

If the present light intensity is low, the probability that two photons hit one micro-cell at the same time (i.e. during the time the micro-cell needs to recharge) is relatively small. However, the SiPM is a strictly non-linear device (the dynamical range is limited by the finite number of pixels). The response can be calculated by the following formula under the assumption of Poisson distributed photon numbers [27]:

$$N_{fire} = N_{total} \cdot (1 - e^{\frac{-PDE \cdot N_{photon}}{N_{total}}}) \tag{2.11}$$

where N_{fire} is the number of fired pixels, N_{total} is the total number of pixels on the SiPM and PDE is the photon detection efficiency. For $N_{photon}/N_{total} \ll 1$, i.e. at low light intensities, the relation is almost linear.

2.3.4 Dark-Rate and Afterpulses

Charge carriers cannot be produced by photon absorption alone. Even if no light is present on the surface, charge carriers can be produced which then trigger an avalanche breakdown resulting in a signal that cannot be discriminated from a real photon-induced signal. The mean dark current or the mean dark count rate can indeed be measured and subtracted from every measured signal. But the variance associated with this value will remain as an unavoidable source of noise. There are two main mechanisms responsible for the dark rate.

- **Thermal excitation:** In some semiconductor materials the band gap is small enough compared to the thermal energy of a charge carrier at room temperature $E_{th} = k_b T = 0.0259\,\mathrm{eV}$ that an electron-hole pair can be generated. For silicon this is not the case since it has an indirect band gap which makes additional momentum transfer necessary. However, thermal excitation is possible in the presence of intermediate states in the forbidden band gap region due to impurities and crystal defects. The resulting transition is a two-step transition over the impurity state. Thermal excitation can be reduced if the device is cooled.

- **Tunnel excitation:** The electric field induced charge carrier excitation, or short "*tunnelling*", is a quantum-mechanical phenomenon. Electrons can be described by their wavefunction giving them a certain probability for tunnelling through the band gap to a state in the conduction band with the same energy (see figure 2.16). The movement of an electron from the p-side to the n-side is prevented by an approximately triangular shaped potential barrier. The height of the barrier is the band gap energy E_G and the width is given by:

  $$L = \frac{E_G}{q_e \mathcal{E}}$$

  where q_e is the electron charge and $\mathcal{E}$ is the electrical field. The probability for a transition through the triangular shaped barrier can be calculated with the WKB[4] approximation [19]:

  $$P_{tunnel} \approx \exp\left(-2\int_0^L \sqrt{\frac{2mE(x)}{\hbar^2}}dx\right) = \exp\left(\frac{-4\sqrt{2m}E_G^{3/2}}{3q_e\hbar\mathcal{E}}\right) \tag{2.12}$$

  Due to the high electric field in the multiplication region of the SiPM, the tunnelling effect plays an important role. It cannot be reduced by cooling like the thermal induced

---

[4] Wentzel-Kramers-Brillouin

dark-current since the high electric field causing tunnel excitation is crucial for avalanche breakdown.

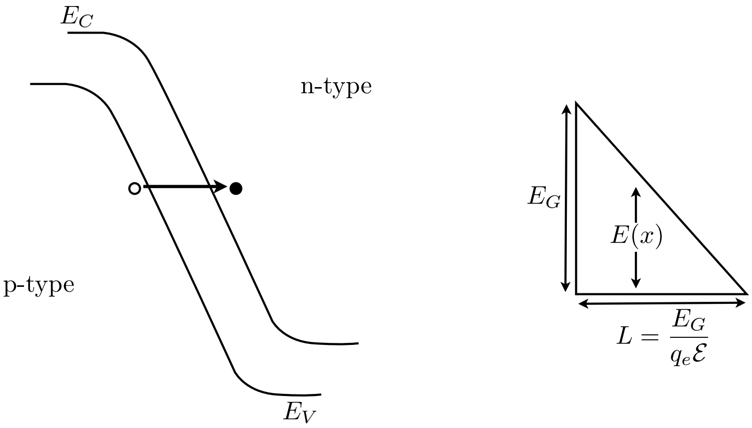

Figure 2.16: Left: Schematic view of the tunnelling effect. **Right:** Shape of the potential barrier used for the calculation of the tunnel probability.

The number of dark count induced events per second is referred to as the dark count rate. It shows an exponential dependence on the electric field according to equation 2.12. Typical values are in the range from several 100 kHz to MHz (see section 3.2 for more details).
Another process which is responsible for noise production is the so-called afterpulsing effect. It is possible that during avalanche breakdown some of the carriers will be trapped by impurity states. After some time they will be released again. If they stay longer in the trap than the recovery of one single pixel, there is a probability for a subsequent Geiger-mode discharge initiated due to the release of this carrier. This will result in a single photon pulse appearing with a time shift to the real signal.

2.3.5 Optical Crosstalk

It is well known that during avalanche breakdown of a reverse biased diode photons are produced [28, 29, 30]. The physical reasons therefore are manifold: carrier recombination, intraband transitions and bremsstrahlung caused by the coulomb interaction of hot carriers. Some photons from the processes mentioned above may have enough energy to generate electron-hole pairs. An often referred number is about 10^{-5} [29] photons per charge carrier crossing the junction. For a representative gain value of $M = 10^6$ this gives about 10 photons per avalanche breakdown. These photons may reach a neighbouring pixel where they can trigger additional avalanche breakdown. Therefore there is a photon assisted crosstalk between the pixels. This undesired effect, often referred to as optical crosstalk, falsifies the obtained signal in a way that the measured signal indicates more photons than really have been observed. An apparent way to reduce optical crosstalk is to isolate optically the individual pixels. This can be achieved by putting trenches between the pixels (see picture 2.17). Optical crosstalk represents especially a problem if the exact number of photons is needed (e.g. for the determination of the PDE).

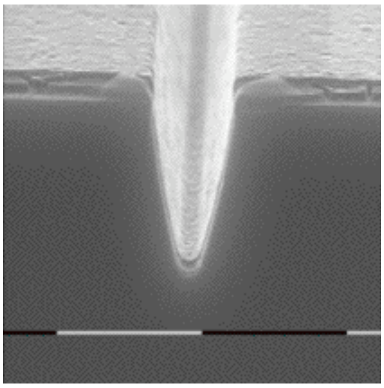

Figure 2.17: Microscopic picture of an optical trench running between the individual pixels [31].

Chapter 3

Silicon Photomultiplier Test-Setup

A test-setup for the characterisation of SiPMs was developed and built in the context of this diploma thesis. Some of the fundamental parameters can be measured which allows to compare devices from different manufacturing companies differing for example in the number of pixels. The actual test setup allows to measure the gain M, the pixel capacitance C_{pixel}, the dark-rate, and the photon detection efficiency.
In the following chapter the experimental setup's for the individual measurements will be explained. First measurement results are presented.

3.1 Gain Measurement

Setup

The gain M was measured as a function of the reverse bias voltage U_{bias} applied to the SiPM by using the setup described in figure 3.1. A blue LED was used as the light source for this measurement. It was placed inside of an extra lightproof box well separated from the SiPM in order to avoid pick-up noise on the SiPM readout circuit. A frequency generator[1] was used to drive the LED by producing every 10 μs a short voltage pulse with a peak amplitude of 10 V and a width of 10 ns. Neutral optical filters (see left side of figure 3.2) are placed behind the

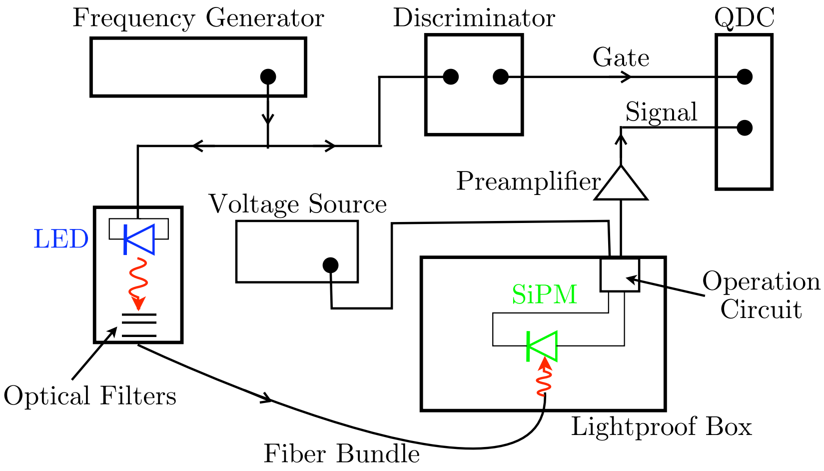

Figure 3.1: Schematic view of the setup used for gain measurements.

---

[1] LeCroy model Model 9109 Arbitrary Function Generator

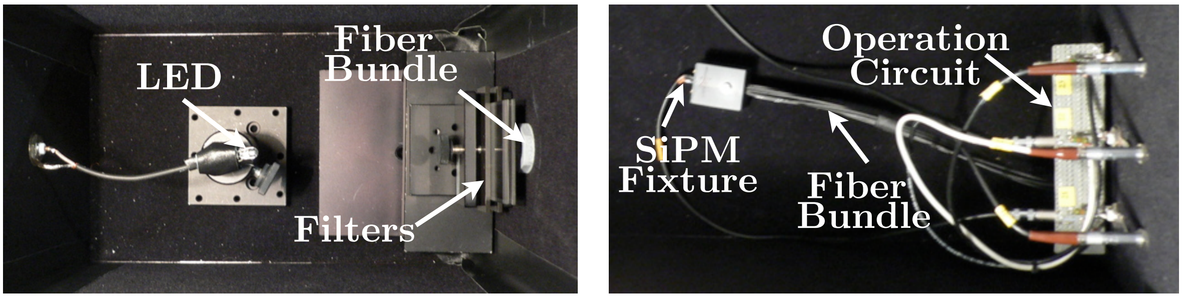

Figure 3.2: Left: Inside view of the lightproof box containing the LED, illuminating one end of the fibre bundle. Neutral filters are used to tune the light intensity. **Right:** Inside view of the box containing the SiPMs and the biasing circuits. A plastic fixture was used to couple the fibre bundle to the active surface area of the SiPM. The signals are passed to the outside through LEMO-connectors.

LED to tune the light intensity in a way that every light pulse contains a few ($O(10)$) photons. An optical fiber bundle consisting of 8 individual fibres covered with photo-resistive coating material guides the light to the active surface of the SiPM which was also placed inside a lightproof box (see right side of figure 3.2). The electrical operation circuit of the SiPM is shown figure 3.3. If the light pulse hits the active surface, an optical current is produced which is converted into a voltage pulse by the $2.7\,\mathrm{k\Omega}$ load resistor. The voltage pulse (typical amplitude $\approx 1\,\mathrm{mV}$) was amplified by a factor of 50 using a fast preamplifier[2]. The amplified pulse was integrated using a 10-bit *Charge to Digital Converter* (QDC)[3] over a time window of $\tau_{integr.} = 80\,\mathrm{ns}$. The integration was triggered independently from the SiPM signal by the frequency generator used to drive the LED. The data acquisition system which was used to read out the measurement data for further processing on a computer was based on the *Computer Automated Measurement And Control* (CAMAC) standard and controlled via USB

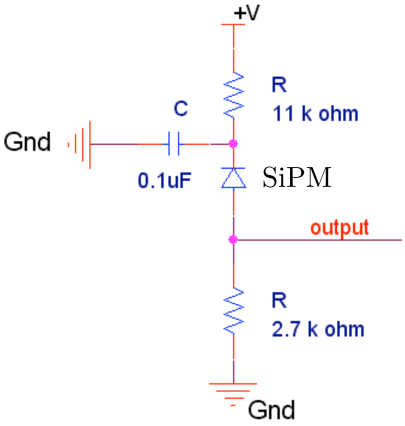

Figure 3.3: Basic connection diagram for the SiPM. The capacitor provides the needed energy when the SiPM goes into breakdown and the $11\,\mathrm{k\Omega}$ resistor limits the voltage drop at the SiPM during breakdown. The $2,7\,\mathrm{k\Omega}$ resistor converts the generated current into a voltage signal at he output.

---

[2] Phillips Scientific, Model 774, Bandwidth: 100kHz-1,5Ghz (3dB)

[3] LeCroy Model 2249A, 12-Channel Charge Integrating ADC

with the Wiener CC-USB CAMAC crate controller. The steering and readout software was written in C++.

Measurements

Figure 3.4 shows a histogram, representing the direct result obtained by the gain measurement setup described above. The number of events is plotted against the pulse charge (in QDC channels) which was integrated by the QDC. It was acquired by calling a program which reads out the charge value of each QDC integration. The acquisition time of a spectra depends on the wanted statistics and takes between 10 and 20 minutes. Each of the visible peaks correspond to a certain number of photoelectrons (pe):

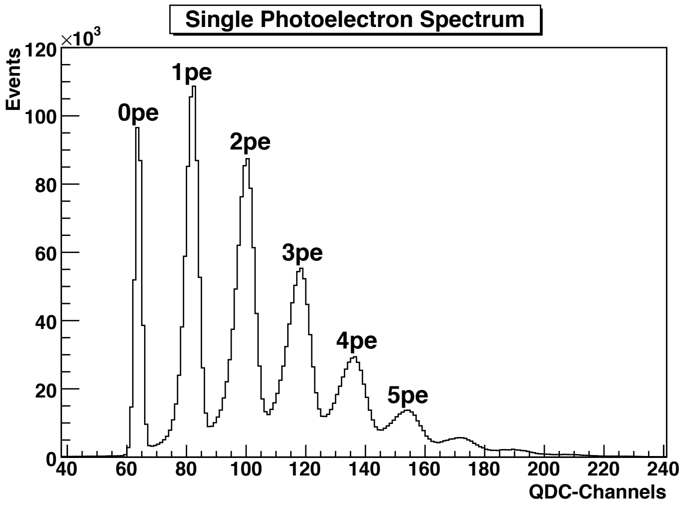

Figure 3.4: Typical photoelectron-spectrum obtained for a certain bias voltage: The number of events is plotted against the charge. Every peak corresponds to a certain number of fired pixels e.g. 0pe: (pedestal), 1pe: 1 photon detected etc.

- The first peak (0pe) is referred to as "pedestal". It represents all events where no photon was detected which means that only noise was integrated. The position of the pedestal can be changed by variation of the integration time or directly by turning a screw on the QDC.
- The second peak (1pe) corresponds to the charge integrated when one photon was detected.
- and so forth...

The sharp separation between the individual peaks shows the excellent single photon resolution and is a result of the uniformity of the micro-cells (pixels) on the device. In other words: the charge laid off at the limited Geiger-mode discharge of a micro-cell is practically the same for all individual micro-cells. The situation is different from the linear amplification process of a PMT or an APD, where the final number of electrons is underlying variations due to statistical fluctuations in the avalanche process.

It is possible to evaluate the gain for the applied bias voltage from figure 3.4 since it is equivalent to the distance between two neighbouring peaks. An apparent way to measure the gain is to apply a Gaussian fit to each individual peak and to subtract the peak-value from two neighbouring peaks. Another way which was used during this thesis is to generate the frequency spectrum of figure 3.4 by applying a *Fast Fourier Transformation* (FFT). The discrete Fourier transformation is defined by the following equation:

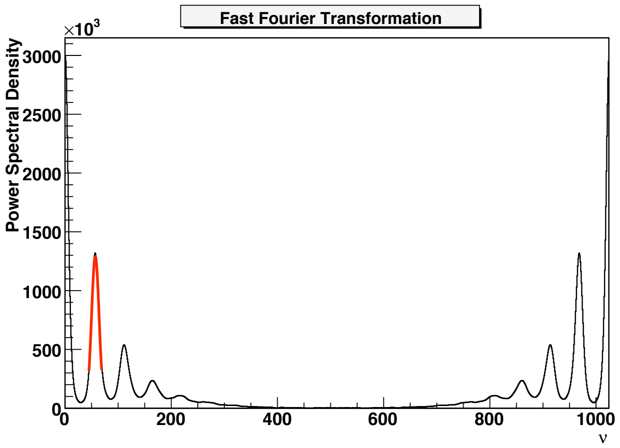

Figure 3.5: Fast Fourier transform of the histogram shown in figure 3.4. A Gaussian fit has been applied (red curve) to the first peak whose position represents the "gain frequency". The subsequent peaks correspond to multiples of the "gain frequency" since the single photoelectron spectrum cannot be described by a single sine-term (i.e. the peaks have different heights).

$$X_k = \sum_{n=0}^{N-1} x_n e^{-\frac{2\pi i}{N}kn} \qquad k = 0, ..., N-1 \tag{3.1}$$

It generates from a series of (in general complex) numbers x_0, ..., x_{N-1} (in this case the values of the histogram bins and $N = 1024$), a series of complex numbers X_0, ..., X_{N-1}. From the definition 3.1 follows the periodicity: $X_k = X_{k+N}$. Under the assumption that the x_k are real numbers (which is here the case) one obtains: $X_{-k+N} = X_{-k} = X_k^*$. Consequently for the real and imaginary part follows:

$$\mathrm{Re}(X_k) = \mathrm{Re}(X_{-k+N}) \tag{3.2}$$

$$\mathrm{Im}(X_k) = -\mathrm{Im}(X_{-k+N}) \tag{3.3}$$

Figure 3.5 shows the *power spectral density*[4] $PSD = X_k \cdot X_k^*$ a function of the frequency ν obtained from the histogram shown in figure 3.4. It indicates a left/right symmetry which is explained by relation 3.2 and 3.3. For the left side of the spectrum ($\nu < 512$) the corresponding gain value can be calculated from the frequency by the formula:

$$\mathrm{M[QDC-Channels]} = 1024/\nu$$

---

[4] The power spectral density is generally defined for electromagnetic or sound-waves. It was used in this case to give the rather abstract term of $|X_k|^2$ an intuitive meaning.

The gain value can therefore be calculated by measuring the position of the first peak which was done by the application of a Gaussian fit. To convert the gain value given in the unit "QDC-Channel" to the unit of elementary charge q_e it was multiplied by the following conversion factor:

$$\frac{\mathrm{M[q_e]}}{\mathrm{M[QDC-Channels]}} = \frac{0.25 \cdot 10^{-12}\mathrm{C}}{50 \cdot q_e} = 31211 \tag{3.4}$$

where the 0.25 pC factor represents the resolution of the QDC (i.e. the charge value belonging to a single channel). The factor 50 in the denominator takes into account the usage of the preamplifier, and q_e is the electron charge.

The gain of SiPMs from different manufacturers has been systematically measured as functions of the applied bias voltage U_{bias}. For every value of the bias voltage a spectrum like in figure 3.4 was acquired and the gain was estimated by applying the FFT. The outcomes are summarised in figure 3.6 which shows the gain as a function of the over-voltage U_{over}. The graph demonstrates the linear dependence on the bias voltage as expected from equation 2.9:

$$M = \frac{C_{pixel}}{q_e} \cdot (U_{bias} - U_{break})$$

Accordingly the pixel capacitance C_{pixel} and the breakdown-voltage U_{break} can be determined by fitting the data shown in figure 3.6 to formula (2.9). C_{pixel} is the slope of a straight line, and the breakdown-voltage is defined as the voltage where the gain becomes one. Table 3.1 summarises the results of the measurements. It can be seen that the obtained results are consistent with formula 2.4:

$$C_{pixel} \propto \frac{A}{d}$$

Device	Number of Pixels	U_{break} [V]	C_{pixel} [fF]
HAMAMATSU S10362-11-025C			
Sample 131	1600	-68.21 ± 0.07	22.47 ± 0.02
Sample 132	1600	-68.38 ± 0.07	23.17 ± 0.02
HAMAMATSU S10362-11-050C			
Sample 163	400	-68.2 ± 0.2	101.8 ± 0.2
Sample 164	400	-68.66 ± 0.07	107.4 ± 0.1
HAMAMATSU S10362-11-100C			
Sample 180	100	-68.34 ± 0.06	314.7 ± 0.2
Sample 181	100	-68.8 ± 0.5	313.3 ± 0.5
SensL SPMScint1000X04			
Sample 713/4	1144	-28.56 ± 0.03	57.78 ± 0.04
Sample 714/4	1144	-28.52 ± 0.04	60.7 ± 0.5

Table 3.1: Summary of the measured quantities. The active surface of all detectors is $1 \times 1mm^2$

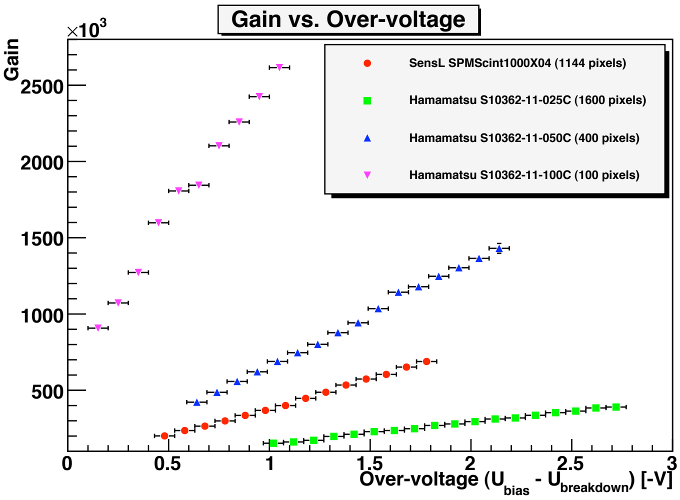

Figure 3.6: Gain as a function of the over-voltage $U_{over} = U_{bias} - U_{break}$ for devices with different pixel numbers (Only the values for one of the two available samples have been plotted for a clearer picture) . As expected the gain is rising with the micro-cell size (smaller number of pixels at constant active area).

3.2 Dark-Rate Measurement

This section describes the measurement of pulse count-rate which is even present in the absence of light. It is important to be measured and compared for different devices since a low dark-rate reduces the noise, allowing to measure the number of photons more precisely.

Setup

The dark-rate measurement was carried out with a modified version of the setup used for the gain-measurement and is shown in the following diagram:

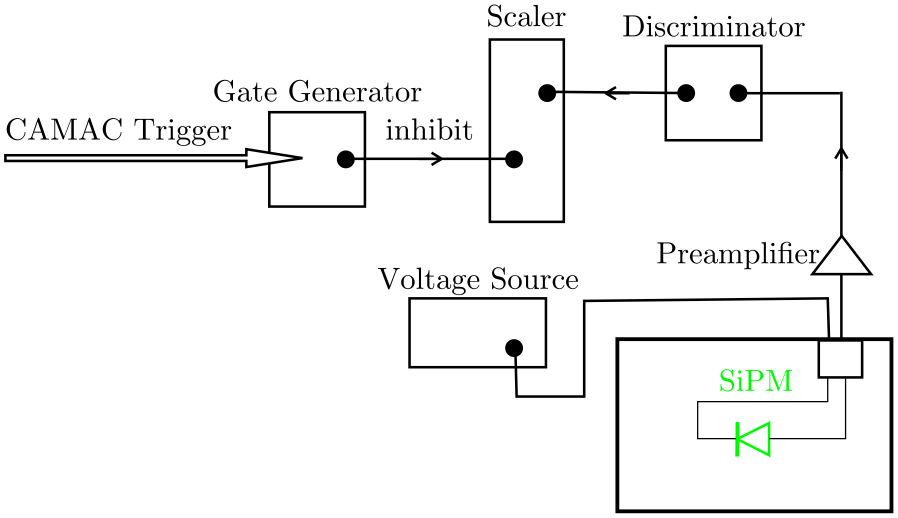

Figure 3.7: Setup used for the dark-rate measurement.

The SiPM was placed inside of a lightproof box in order to avoid photon induced signal pulses to be produced. The SiPM signal was amplified by a factor of 50 and guided to a discriminator. To find the correct value for the discriminator threshold the SiPM signal was measured with an oscilloscope (figure 3.8). The signals belonging to one, two and three photoelectrons can be clearly separated. The amplitude of a two-photoelectron pulse has twice the amplitude of a single photoelectron signal and so forth. In order to be sensitive to all pulses during measurements of the dark-rate, the discriminator threshold was set to the half of the single photoelectron signal (0.5pe threshold). If the signal amplitude at the discriminator input is larger than the chosen threshold value, a 4 ns broad logical pulse is generated and guided to the input channel of the CAMAC scaler module[5]. The scaler counts the number of incoming pulses as long as no signal is present at the inhibit input. The inhibit signal is generated by a gate generator[6] and was interrupted for a well defined interval of $t = 1\,\mathrm{s}$ if the gate generator received a trigger signal from the CAMAC crate controller. When the gate ends, the number of counted pulses is subsequently read out by the controller and represents (with some corrections, see below) the dark-rate.

---

[5] LeCroy Model 2550B, 100MHz Scaler

[6] CAEN Model V93B

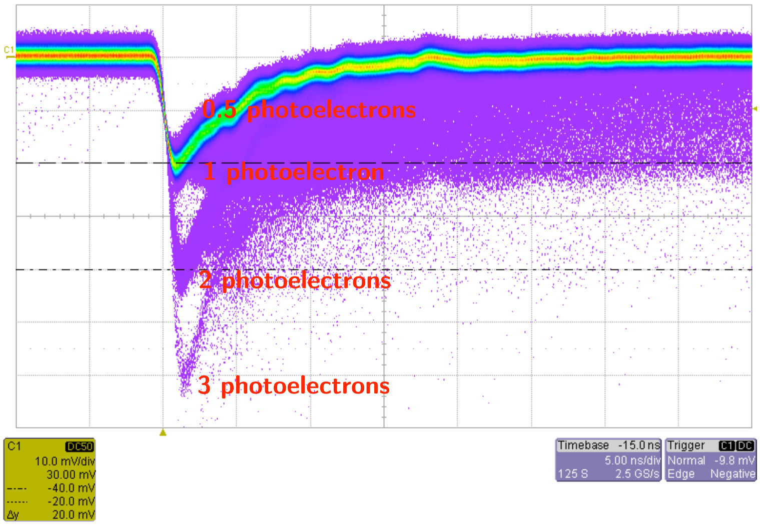

Figure 3.8: SiPM signal in the absence of Light. Signal pulses corresponding to one, two and three pixels firing (photoelectrons) can be seen. The vertical division is 10 mV and on horizontal division is 5 ns.

Dead time correction

The used scaler module showed a dead time of $\tau_{dead} = 10\,\text{ns}$. This means that two subsequent pulses could be separated by the scaler if the time interval between them was larger than the dead time interval. If the time difference was smaller than this value the subsequent pulse was not recognised. Hence at high frequencies the measured rates are smaller than the real dark-rate. Therefore the measured rates were corrected using the non extended dead time formula (3.5). It assumes that the insensitive time is not extended if a second pulse appears within the dead time generated by the first pulse.

$$R_{real} = \frac{r}{1 - r \cdot \tau_{dead}} \tag{3.5}$$

where r is the measured dark-rate and R_{real} represents the real (corrected) value.

Measurement Results

The dark rate was measured as a function of the applied over-voltage for the different SiPM samples. Figure 3.9 shows the result for a discriminator threshold value corresponding to half a single photoelectron signal (0.5pe). As expected the number of dark counts is increasing with the over-voltage since the probability for an electron to tunnel into the conduction band is rising with the applied electric field in the depletion region (see equation 2.12). The measurements show that the dark-rate is increasing with increasing pixel size and the two samples from SensL in general show a higher dark-rate then the devices from HAMAMATSU. However, there are more measurements needed in order to explain the the exact shapes of the curves; e.g. the flattening for high rates for the two SensL devices and the rise for high over-voltages of the MPPCs.

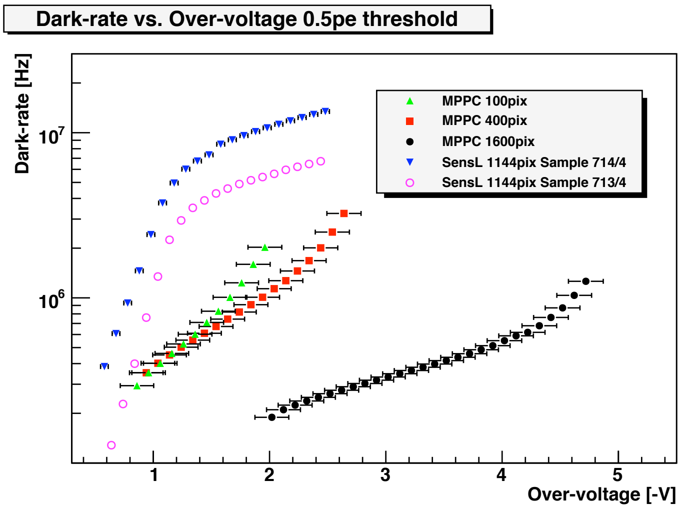

Figure 3.9: Dark-rate as a function of the over-voltage U_{over} for several devices from the companies SensL and HAMAMATSU (MPPC) with different pixel numbers. Only for the devices from SensL the measured values for both samples have been plotted since they differ significantly. Two different values for the voltage errors bars are visible since different voltage sources were used for the measurements.

Dark-rate Spectrum

A pulse height spectrum of the dark-rate pulses can be measured by keeping the over-voltage constant and varying the discriminator threshold. Figure 3.10 shows the representative result for a MPPC with 1600 pixels and $U_{over} = 2.44\,\mathrm{V}$. It can be seen that the dark-rate is

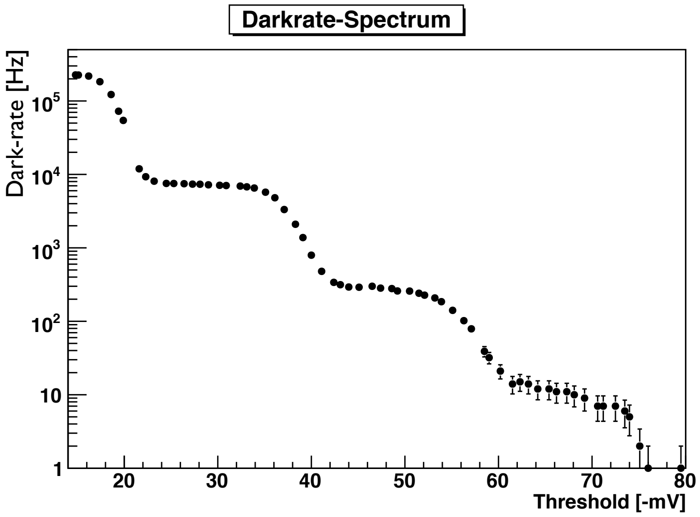

Figure 3.10: MPPC with 1600 pixels: Dark-rate as a function of the voltage threshold. $U_{over} = 2.44\,\mathrm{V}$

decreasing strongly with an increasing discriminator threshold. This shows that the devices are in particular suitable for applications where the signal threshold can be set higher than the single photoelectron threshold, e.g. in PET applications where the signal is rather large

(several hundreds of photoelectrons).
The curve shows a characteristic stair-like shape due to the high pulse height uniformity for a fixed number of pixels firing. It allows to determine the pulse amplitudes belonging to the signal of a certain number of pixels. One can determine a single photoelectron pulse amplitude of about $A_{1pe} = 20\,\mathrm{mV}$, the 2 photoelectron pulse has an amplitude of $A_{2pe} = 40\,\mathrm{mV}$ and so forth. The fact that there are pulses with photoelectron numbers bigger than one is a hint to the optical crosstalk (section 2.3.5) since the probability for a simultaneous thermal- or tunnel-excitation from electrons to the conduction band for at least two individual pixels by accident is expected to be rather small.

3.3 Photon Detection Efficiency Measurement

One of the most important parameters of a photodetector is the *Photon Detection Efficiency* (PDE), and hence its study is crucial for a complete characterisation of SiPMs. This section describes the actual state of the measurement setup for the photon detection efficiency.

3.3.1 Experimental Setup

The measurements were performed according to the setup shown in figure 3.11 and 3.12. In the following the different components of the setup and their usage will be explained.

75W Xenon Arc Lamp

The used light source was a Xenon Arc lamp. It has an approximately flat and highly stable irradiance in the wavelength region from 400 nm up to 1400 nm. As the stability of the irradiance over a longer time period is crucial in order to compare the measured outputs of the two light detectors it was measured using the calibrated PIN-diode. The PIN-diode was illuminated by the Xe-lamp and the photocurrent was measured every 10 seconds over a time period of five hours. The result of this measurement is shown on the left side of figure 3.13 in a histogram. One can see that the light-intensity is stable over a long period. In particular a drift of the light intensity can be excluded.

Monochromator

In order to measure the spectral PDE as a function of the wavelength, it is needed to select a small wavelength interval out of the continuous light output of the Xenon lamp. For this purpose a grating monochromator was used. It has a scale on its top where a wavelength value can be set by turning a small handle and only light within a narrow bandwidth around the chosen wavelength is present at the exit of the monochomator. The physical operation principle is based on the spatially separation of light of different wavelength. The grating inside the monochromator is illuminated through a small entrance slit, and the diffractive pattern is projected to an exit slit which allows only the first grating order $m = 1$ of a wavelength λ_1 to exit. However the grating equation for constructive interference is also satisfied for wavelengths in higher grating order (e.g. for $\lambda_2 = \lambda_1/2$ for $m = 2$ etc.). Therefore the other wavelengths in higher orders need to be blocked by additional filters. Three filters with different "cut-off" wavelengths ($\lambda_{cut} = 400, 500, 645$) were available which could be

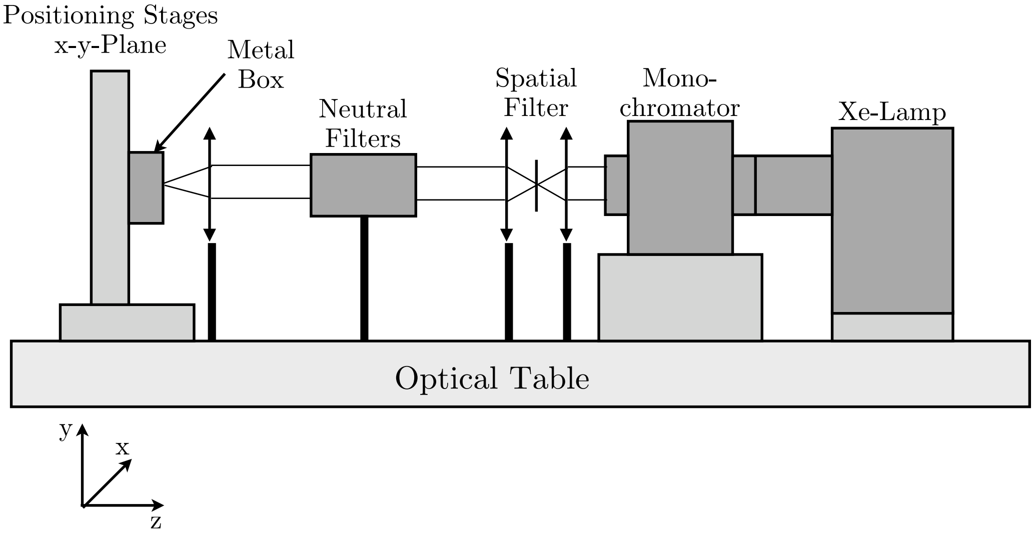

Figure 3.11: Setup for the measurement of the photon detection efficiency.

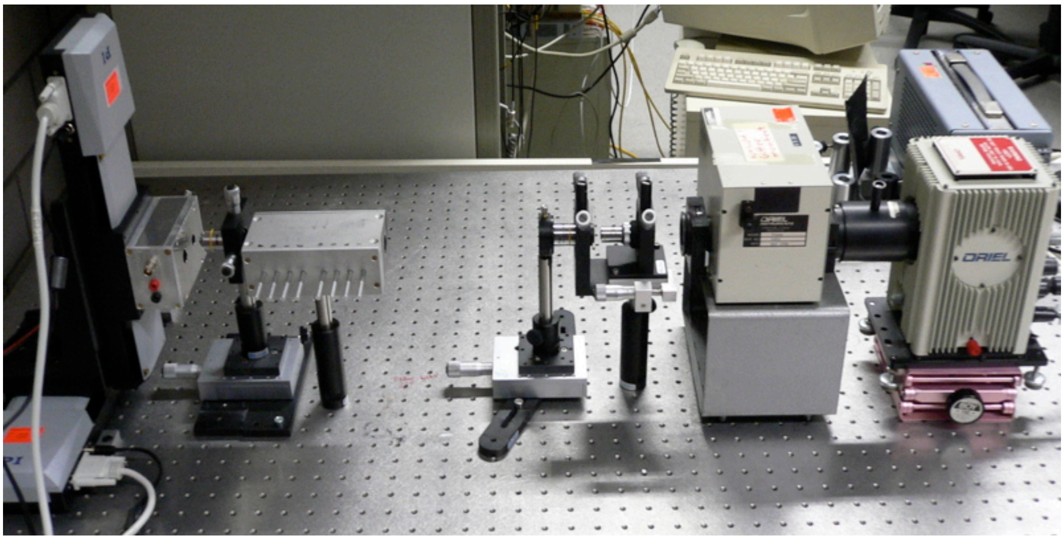

Figure 3.12: Photograph of the setup

inserted to the light path if needed to block all wavelengths λ with $\lambda < \lambda_{cut}$. The reflective grating which was mounted had 1200 lines/mm and could be used for measurements in the wavelength region from 450 nm to 1000 nm (i.e. in the region where the amount of light in the first grating order is high). To calibrate the scale and to determine the bandwidth of the monochromator a Hg(Ar) spectral calibration lamp was used. It has two characteristic lines at 577 nm and 579 nm. The intensity-versus-wavelength profile was measured for two different settings of the entrance and the exit slit width and is shown in figure 3.13. Gaussian fits have been applied to the peaks to obtain the peak position. The peak positions are shifted by 2.7 nm in respect to the wavelengths of the two characteristic lines. The bandwidth, represented by the width of the peak is in the order of $\approx 1 - 2$ nm depending on the actual slit width. However a small slit width has the drawback of a small light intensity which makes the optical alignment difficult and decreases the signal to noise ratio when using a detector which has no internal amplification (PIN-diode). A HeNe-Laser was used for calibration purposes, too. The intensity was not stable enough to measure its profile as it was done for the calibration lamp. Nevertheless the measured value for the wavelength shift could be confirmed by observing the light intensity on a screen which was placed behind the monochromator exit. Therefore the scale was assumed to be globally shifted by 2.7 nm.

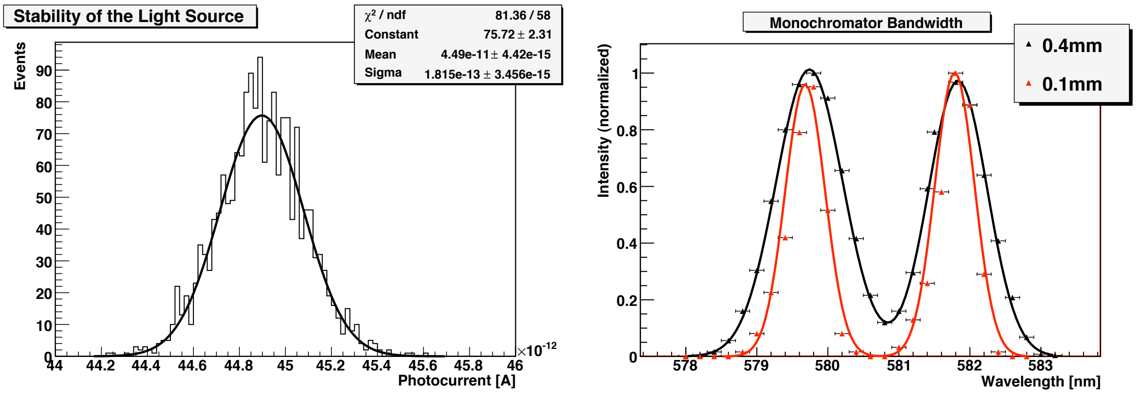

Figure 3.13: Left: Variation of the PIN-diode photocurrent over a time period of five hours. One can see that there is no drift in the light intensity even over a long time period. **Right:** Bandwidth of the monochromator for two different settings (0.1 mm and 0.4 mm) of the entrance and exit slits.

Spatial Filter

The light at the exit of the monochromator is diverging. Additionally the intensity is not homogeneous but shows bright and dark spots due to the scattering of dust particles or dirt and scratches on the lenses. To alter the structure of the light spot, a spatial filter was used. It consists of two microscope objectives and a $\varnothing 5\,\mu$m pinhole in the focal plane. In this way a light spot with a Gaussian intensity profile and with a size down to theoretically $\varnothing 5\,\mu$m can be produced.

Calibrated PIN-photodiode

The used light source has to be calibrated in order to calculate the PDE of the SiPM. A calibrated PIN-diode was used for this purpose. It has an active surface of $3 \times 3\,\mathrm{mm}^2$ and was supplied with individual calibration data in the wavelength region from 350 nm to 1070 nm in the form of a table and a graph which is shown in the appendix A.1. The calibration was performed without applied bias voltage; therefore it was also used without any bias applied.

Picoampere Meter

The picoampere meter[7] fulfills two tasks. The first is to measure the photo-current of the PIN-photodiode and SiPM when illuminated, secondly it was used as a voltage source to supply the SiPM with the appropriate reverse bias voltage. All possible measurement functions could be set manually with the buttons on the front side, as well as over a serial connection to the lab computer. Therefore the program LABVIEW was used under usage of the supplied instrument drivers. The picoampere meter was connected to the PIN-photodiode and the SiPM using a triax-cable in order to reduce noise, especially when measuring small currents. The current from the PIN-photodiode is small due to the missing internal amplification compared to the SiPM. Typical values are in the range of $\approx (10 - 120)\,\mathrm{pA}$. At the smallest measurement range (up to 2 nA) the accuracy of the picoampere meter is 0.3 % of the reading plus 400 fA.

Metal Box

A small metal box (see figure 3.14) was built and serves as a shielding for the PIN-photodiode, the SiPM and the corresponding biasing circuits. For the SiPM a circuit, similar to the one used for the gain-measurement, shown in figure 3.3 was used. Only the $2.7\,\mathrm{k\Omega}$ output resistor was removed since in this setup, the current was measured. Two holes are drilled into the box so that the sensors can be illuminated. Triax connectors and banana jacks are mounted on the sides for the connection with the picoampere meter.

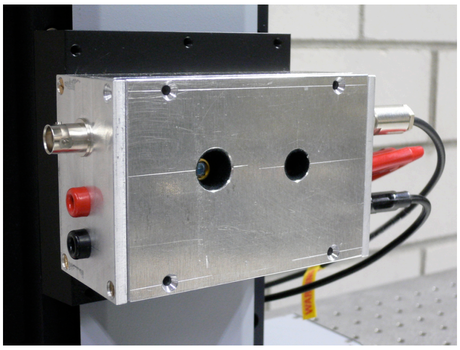

Figure 3.14: Photograph of the metal box housing for the optical sensors mounted on the linear stage. The two sensors could be alternately placed in the light beam path. On the side the cable connectors (triax and banana jacks) are visible.

---

[7] Keithley Model 6487 Picoammeter/Voltage Source

Micrometer Positioning Stage

The micrometer positioning stage carries the metal box with the photon sensors inside. It can accomplish movements in the x-y-plane with a bidirectional reproducibility of $1\,\mu$m. In this way the light beam can be centred on both sensors in a reproducible way.

3.3.2 Measurements

The light spot was centred on the SiPM and on the PIN-diode by moving them in the x- and y-direction while measuring the current. The result of such a scan is shown in figure 3.15. From this measurement, the diameter of the light spot can be determined using:

$$d_{spot} \approx x_2 - x_1 - \mathrm{d}_{\mathrm{SiPM}} \tag{3.6}$$

where x_2 and x_1 are the positions where the current starts to rise and $\mathrm{d}_{\mathrm{SiPM}} = 1\,\mathrm{mm}$ is the side length of the active surface of the SiPM. For the PDE-measurement it is important to know the diameter of the light spot and, if needed, to change it since light could be lost if the spot size is too large (larger than $\approx 1\,\mathrm{mm}$). In this case the whole light would be detected by the PIN-diode since it has a 9 times larger active surface, but the SiPM would only measure a fraction of the total light and therefore the evaluated sensitivity would be too small. From the scan in figure 3.15 a value for d_{spot} of about $\approx 0.7\,\mathrm{mm}$ was measured.

Another very important aspect which has to be taken into account is the non-linear response (see equation 2.11) of the SiPM for a huge number of photons. Therefore the light intensity has to be small which is in conflict with the response of the PIN-diode. It generates only a small current, and therefore the signal-to-noise ratio decreases when decreasing the light intensity. To achieve the best result the intensity was chosen as large as possible while assuring that the SiPM response is linear. To prove the linearity, the neutral optical filters (figure 3.11) were used. The individual attenuation factors were estimated by using the PIN-diode since its response is linear over a wide range. The filters were placed in the light beam path, and the photocurrent-ratio with and without filter was measured, representing the attenuation

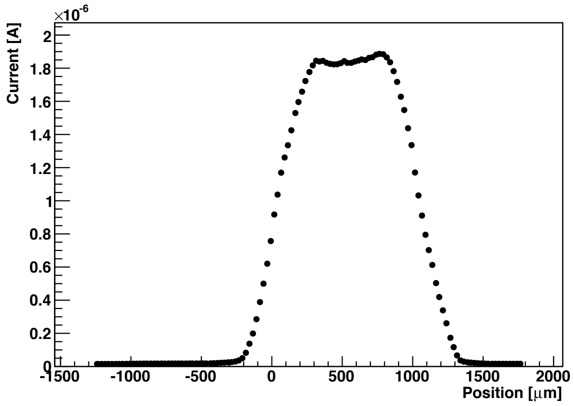

Figure 3.15: Representative scan of a SiPM in the x-direction. The centre of the diode is at $\approx 600\,\mu$m. The diameter of the light spot can be approximated by the width of the peak (the points where the current starts to rises) since the size of the active surface is known to be 1mm.

factor. Then the response curve of the SiPM could be measured. It is shown in figure 3.16. The response can be assumed to be linear up to a photocurrent value of $\approx 6\,\mu$A with respect to the PIN-diode measurement. Considering this value the PDE value could be calculated as follows:

$$PDE = \frac{n_{p.e.}}{n_p} \tag{3.7}$$

where $n_{p.e}$ is the number of photoelectrons per time and n_p is the number of photons per time present on the detector surface. The number of photoelectrons per time can be calculated by measuring the photocurrent I_{SiPM}:

$$n_{p.e.} = \frac{I_{SiPM}}{M \cdot q_e} \tag{3.8}$$

M is the gain and q_e is the electron charge. This represents a approximation since the measured photocurrent I_{SiPM} is artificially increased by afterpulse and crosstalk events. The number of photons n_p can be calculated using:

$$n_p = \frac{P}{h\nu} = \frac{P \cdot \lambda}{hc} \tag{3.9}$$

where P is the optical power and λ is the light wavelength. The optical power P can be calculated by the usage of the calibration data which is given as the responsivity R of the PIN-photodiode (see A.1):

$$R = \frac{I_{pin}}{P} \Rightarrow P = \frac{I_{pin}}{R} \tag{3.10}$$

Hence we get:

$$PDE = \frac{I_{SiPM} \cdot hc \cdot R}{M \cdot q_e \cdot I_{pin} \cdot \lambda} \tag{3.11}$$

In this way the PDE was calculated for the MPPC with 1600 pixels. The result is shown in figure 3.17. The sensitivity is high in the blue region and drops for larger wavelengths as it is specified by the manufacturer. The errors were calculated using the Gaussian error propagation formula. The uncertainty in the calibration data of $\Delta R/R = 5\%$ represents the largest error source.

The task of this thesis was to design and to built a test-setup for the characterisation of SiPMs. The functionality of the setup was proven by systematic measurements of the gain, the dark-rate and the PDE. Eight samples with a active surface of $1 \times 1\,\mathrm{mm}^2$, from two different manufacturers have been tested. The pixel numbers of the devices range from 100 to 1600 per mm^2. The measured gain shows as expected a linear dependence on the applied bias voltage and ranges between $10^5 \lesssim M \lesssim 3 \cdot 10^6$, depending on the applied bias voltage and the pixel size (see figure 3.6). The values for the measured dark-rate range between $(1 - 100) \cdot 10^5\,\mathrm{Hz}$. However, it was shown that the dark-rate decreases significantly when setting a higher counting threshold. Therefore the devices can be used without constraints in applications where the signals are large. A first measurement of the PDE for a MPPC with 1600 pixels was possible. Studies to estimate the error introduced by crosstalk and afterpulse effects are planned, which were not possible in the context of this thesis. In addition there are systematic measurements needed like measurements of the dependence of the PDE on the applied bias voltage to draw precise conclusions.

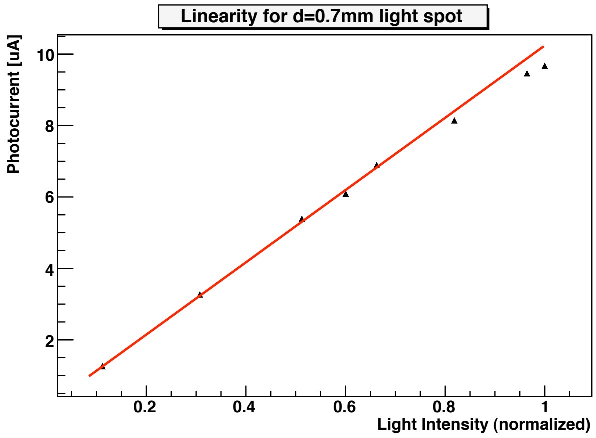

Figure 3.16: Measured photocurrent of the MPPC as a function of the light intensity for a $d_{spot} = 0.7\,\mathrm{mm}$ light spot. The response is linear up to a current of $\approx 6\,\mu\mathrm{A}$.

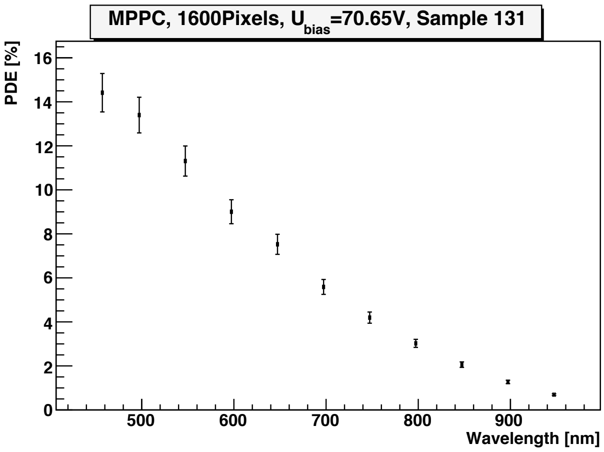

Figure 3.17: Measured PDE for the MPPC with 1600 pixels (including crosstalk and afterpulses). The maximum sensitivity lies in the blue region and falls down for longer wavelengths. The error bars were calculated according to the Gaussian error propagation formula. The largest error source is the uncertainty of the calibration of the PIN-diode ($\Delta R/R = 5\%$).

Chapter 4

Application of Multi-Pixel Photon Counters to Positron Emission Tomography

The previous parts of this thesis were dedicated to the general characterisation of SiPMs. In the following, emphasis will be on the application of the SiPM to *Positron Emission Tomography* (PET) which is a non-invasive medical imaging technique used for the monitoring of active regions in organisms. It refers to the technique of functional imaging and can be very helpful in finding cancer cells since it provides a picture of the patient indicating regions of high metabolism. Therefore it has become a very powerful tool in the modern clinical diagnostics. The working principle is as follows: A positron emitting radionuclide (β^+ active) is incorporated into a so-called tracer molecule (e.g. glucose or another substance involved in the metabolism of the organism). The substance marked in this way, often referred to as "radiotracer" is then injected into the patient where it localises according to the physiologic properties. More precisely the glucose molecules will be used by all cells, but more glucose will be used by cells having an increased metabolism (e.g. cancer cells). Since the β^+ decay is a three body decay (${}^{\mathrm{A}}_{\mathrm{Z}}\mathrm{X}_{\mathrm{N}} \rightarrow {}_{\mathrm{Z-1}}{}^{\mathrm{A}}\mathrm{X}'_{\mathrm{N+1}} + \mathrm{e}^+ + \nu_{\mathrm{e}}$), the positrons are emitted with a certain energy distribution showing a maximum energy depending on the used radionuclide [32] ($\mathrm{E}_{\mathrm{max}} = \left[\mathrm{m}({}^{\mathrm{A}}\mathrm{X}) - \mathrm{m}({}^{\mathrm{A}}\mathrm{X}') - 2\mathrm{m}_{\mathrm{e}}\right] \mathrm{c}^2$). These positrons lose energy while propagating in the surrounding tissue until they reach thermal energy and annihilate with electrons from the tissue, forming two 511 keV photons moving in anti-parallel directions because of energy-momentum conservation. Scintillating crystals coupled to photodetectors are arranged in a ring-like geometry (see figure 4.1) and are used to detect the 511 keV photons. The scintillating crystals convert the gamma rays into visible light which can be detected by photodetectors like PMT's or APD's. If two gamma rays are detected within a certain time window (typical value $\approx$ 12 ns)[33] the radionuclide is expected to lie on a line joining the two detector elements. This line is called *Line of Response* (LOR). The reconstruction algorithm [34] produces an image of the radiotracer concentration by searching for regions where an increased number of LOR's are crossing compared to other regions. In general there exist two different data sampling methods [34]:

- **Two-dimensional sampling:** Only LOR's with polar angle $\theta = 0$ (see figure 4.1, right) are sampled and the reconstructed image is obtained by putting together the acquired data for different values of the z-coordinate.
- **Three-dimensional sampling:** The polar angle can be opened up to a desired value. However, this is a trade-off between sensitivity gain, meaning that more data can be sampled without increasing the radiation dose, and an increase of background events from Compton-scattering events due to the longer travel path of the photons. Further-

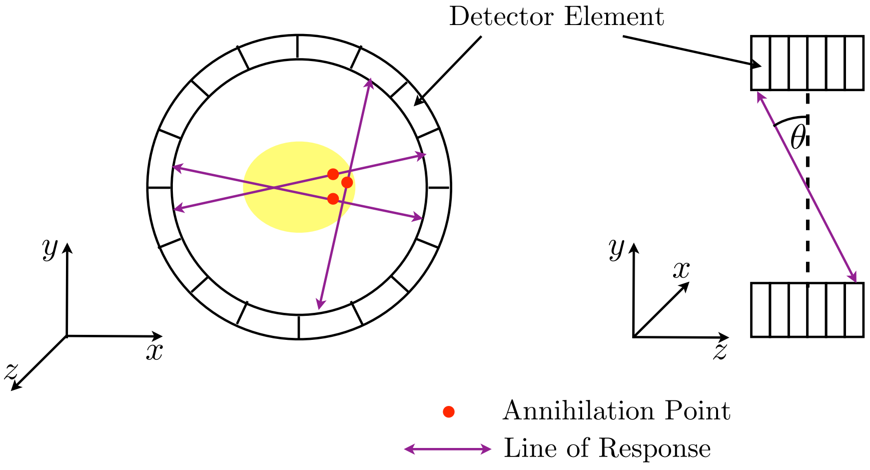

Figure 4.1: Schematic structure of a PET detector. **Left:** XY-view of a PET detector. The area where many lines cross represents an area of increased metabolism. **Right:** YZ-view of adverse detector elements. In 2-dimensional PET all data are sampled with polar angle $\theta = 0$ while in the 3-dimensional case this is extended to measuring projections with $\theta > 0$.

more three-dimensional data taking is only possible if the resulting higher coincidence rates can be processed by the hardware.

The spatial resolution (typical value of a clinical PET $\approx 4 - 6\,\mathrm{mm}$) of such a detector is limited by the positron range (see table 4.1) and the non-collinearity of the two annihilation photons due to the momentum of the electron and positron when annihilating. These effects cannot be improved by better detectors. The β^+-emitting radionuclide is chosen in a way to keep the radiation exposure for the patient as low as possible and being suitable for the specific application. Table 4.1 lists the properties of the most common radionuclides used for PET. Due to the relative short half life $\tau_{1/2}$ these radionuclides have to be produced on-site with a cyclotron by collisions of protons or deuterons on a target. Most of today's PET systems use PMT's for the detection of the scintillation light. Among the advantages of these devices like a high gain and the mature technology there are also disadvantages like their sensitivity to magnetic fields which is the reason why they cannot be used in combination with *Magnetic Resonance Imaging* (MRI) tomography. Their bulky shape is limiting the granularity and thus the spatial resolution of the PET-detector. There are also concepts to use APD's for this purpose but this brings the drawback of rather sophisticated readout electronics due to

Radionuclide	$\tau_{1/2}$ [min]	E_{max} [MeV]	R_{mean} [mm]	R_{max} [mm]
^{15}O	2.03	1.738	2.5	7.3
^{13}N	9.96	1.197	1.5	5.1
^{11}C	20.4	0.959	1.1	4.1
^{18}F	109.8	0.633	0.6	2.4

Table 4.1: Half life, maximum energy, mean distance and maximum free path of positrons (in water) of radionuclides mainly used in PET [34].

the relative small gain. In contrast the SiPM has all the necessary properties for the PET application and therefore seems to be an appropriate candidate. The work shown in this part of the thesis was carried out at the *Deutsches Elektronen Synchrotron* (DESY) in Hamburg. A two channel setup was built up which allowed an investigation of the energy resolution $\Delta E/E$ and the timing resolution Δt when using SiPMs for the crystal read-out. Parts of the presented results will be published in [35].

4.1 Physical Principles of PET

For the functionality of a PET detector several physical effects are important. This section gives a brief introduction of the basic principles used.

Photon Interactions with Matter

As it was explained in section 1.2, photons mainly interact with matter in three different ways. The linear attenuation coefficient $\alpha(E)$ for the individual interaction types and the total value are shown in figure 4.3 as a function of the photon energy for Sodium Iodide (NaI) which was formerly often used for PET cameras. Using $\alpha(E)$, the attenuation of radiation intensity as a function of the material thickness is described by formula:

$$P(x) = P(0) \cdot e^{-\alpha(E)x} \, ,$$

where $P(x)$ is the intensity after passing material with a thickness of x. The photons resulting from the positron annihilation in PET have an energy of 511 keV. Figure 4.3 shows that for this energy, photoelectric effect as well as compton scattering is important. The pair production is prohibited due to the energy threshold of $E_\gamma \gtrsim 2m_e$ and therefore plays no role for PET. The first step in the detection of a gamma ray is the transfer of energy to an electron. The expected energy distribution for electrons from the photoelectric effect or Compton scattering is shown in figure 4.2. It can be separated into two parts: the Compton continuum arising from the continuous energy transfer to the electron described by formula 1.3 and a clear peak (photopeak) since the energy transferred to the electron by photoelectric absorption is discrete and unique. For the detection of gamma-rays the photoelectric effect is desired since the whole energy is transferred to the electron whereas in the case of Compton scattering only a fraction of the energy is transferred and the remaining photon may be lost.

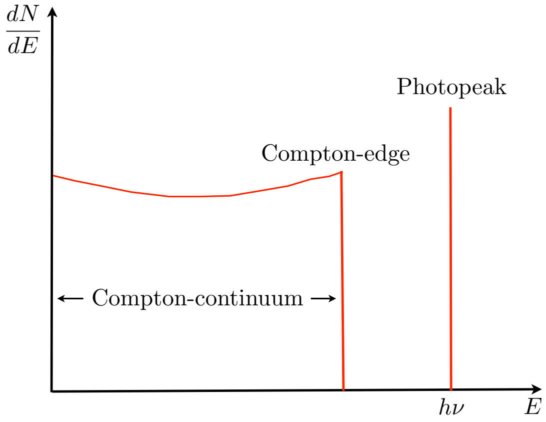

Figure 4.2: Idealised energy spectrum of electrons from Compton scattering and photo absorption

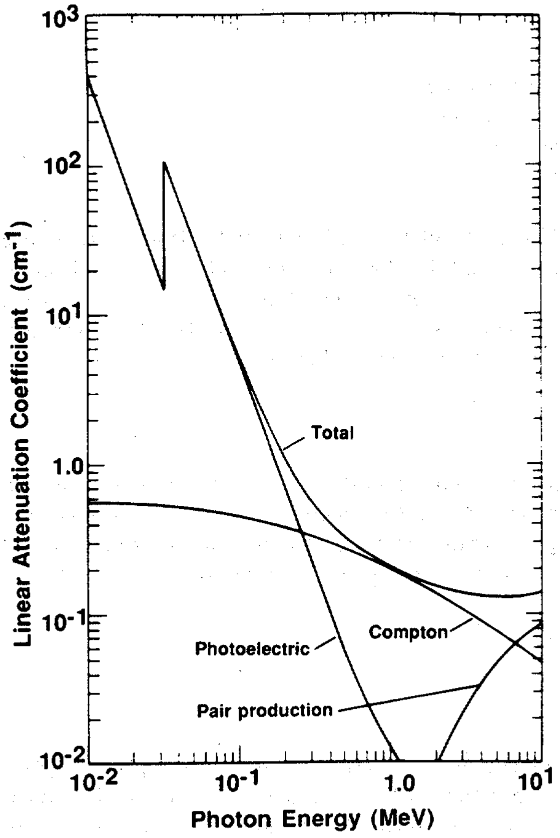

Figure 4.3: Linear attenuation coefficient of NaI as a function on the photon energy. For low energies the photoelectric absorption is dominating. The characteristic discontinuity represents the energy threshold where the excitation of a K electron becomes possible [8].

Photon interactions with scintillators

The 511 keV photons from the positron annihilation have to be converted into visible light in order to be detectable by a standard photodetector like a PMT, APD or a SiPM, respectively. Inorganic scintillators are used for that purpose due to the higher density (higher Z) than organic scintillators resulting in a higher probability for the desired photoelectric absorption (equation 1.2). The higher stopping power reduces the crystal dimensions and therefore allows more compact systems. The gamma rays can interact with the electrons in the scintillator via the photoelectric or the Compton effect, and the resulting free electrons can excite other electrons and hence produce scintillation light. The process of scintillation light production is schematically described in figure 4.4. The passage of a charged particle excites an electron from the valence band to the conduction band. If there would be no activator states (small amount of impurities) the electron would subsequently fall back to the ground state under emission of a photon offering exactly the energy needed for further excitation. If activator states are present the electron will rapidly make a non-radiative transition to an activator state. The photon resulting from the subsequent transition will therefore not have enough energy to excite ground state electrons and can pass the crystal without absorption. The properties of common types of scintillation crystals used for PET are listed in table 4.2. In the early 1990's, the most commonly used scintillators for PET were BGO[1] and NaI. Where BGO has the advantage of not being hygroscopic or fragile like sodium iodide (NaI) and its stopping power is larger compared to NaI. However the decay time is longer. During the 1990's the new scintillators LSO, LFS[2] and related materials like YLSO have been developed [36] which are now commercially available and show good properties for the PET application. The light yield for LSO is higher than for BGO, and the decay time is much shorter allowing a better timing resolution, important for improvements of the detector performance, as it will be discussed in the following sections.

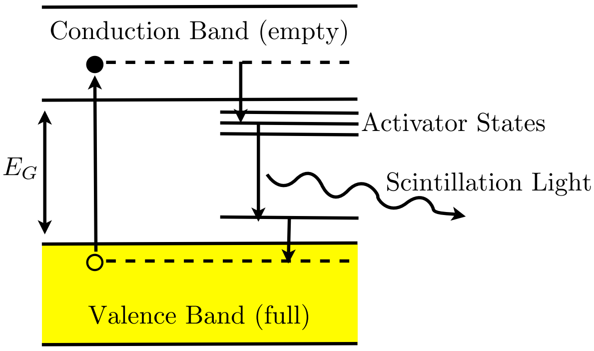

Figure 4.4: Schematic-al illustration of the scintillation light production. An electron becomes excited via ionisation of a passing charged particle. Subsequently it performs a non radiative transmission to the activator states slightly below the Conduction band before making a radiative transition to states slightly above the valence band. Hence the emitted photon hasn't enough energy to excite electrons from the ground state and can pass the crystal without being absorbed.

Photons can interact in the scintillator in different ways as it was already mentioned above.

---

[1] Bismuth germanate

[2] Lutetium Fine Silicate

Scintillator	Decay time [ns]	Peak emission wavelength [nm]	Light yield [% of NaI]	Thickness for 90% efficiency at 511keV [cm]
NaI(Tl)[a]	230	410	100	6,6
BGO[b]	300	480	15	2,4
LSO[c]	40	420	75	2,7
BaF_2[d]	0.6	220	5	5,1

---

[a] Sodium iodide doped with thallium

[b] Bismuth germanate $Bi_4Ge_3O_{12}$

[c] Lutetium oxyorthosilicate doped with cerium $Lu_2SiO_5 : Ce$

[d] Barium Fluoride

Table 4.2: Properties of commonly used inorganic scintillators for PET. [34]

Some of the different types of gamma ray interactions are shown in figure 4.5. It shows a scintillation crystal which is wrapped with a reflective material in order to collect more visible scintillation light while the right side was left open for attaching the photodetector.

- The first interaction (from top to bottom) shows a photon which transfers its entire energy to an electron via photoelectric interaction. The resulting free electron may lose energy due to ionisation and hence produces scintillation light as described above.
- The second interaction shows an annihilation photon which scatters off an electron and then escapes from the scintillator. In this case only a fractional amount of the 511 keV photon energy is deposited in the crystal and hence a smaller amount of scintillation light will be produced compared to photoelectric absorption.
- The third gamma ray scatters, but stays inside the crystal where it finally assigns its energy to an electron. Therefore the whole energy is deposited in the crystal.
- The fourth gamma ray performs a multiple scattering which can produce scintillation light with an energy between the Compton edge and the photo-peak in figure 4.2.
- The fifth gamma ray scatters off an electron from the surrounding material before it enters the crystal and hence is called a backscatter event.

The weight of the different interaction types depends on the scintillating material and on the size of the crystals; e.g in small crystals, often only a fraction of the total energy will be deposited (second gamma ray), whereas in larger crystals the probability for depositing the whole energy is higher (third gamma ray).

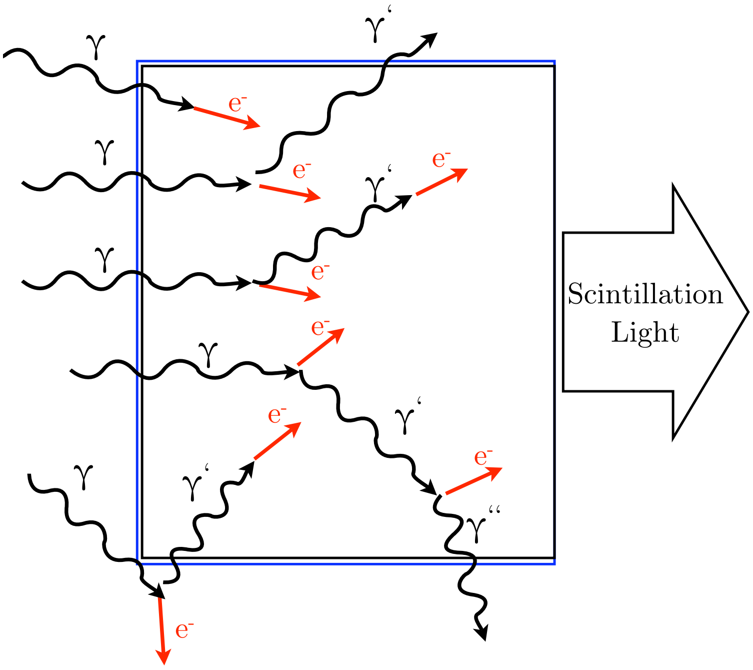

Figure 4.5: Different interactions of gamma rays in a scintillation crystal resulting in detectable scintillation light.

Inorganic scintillators show an intrinsic energy resolution which has two main causes:

Inhomogeneities and impurities: Due to the production process inhomogeneities and impurities cannot be fully avoided, and hence photons produced at different positions inside the crystal will give different response in form of light detected by the photodetector.

Nonlinearities: If the energy response of the crystal is not strictly linear (i.e. the proportionality factor depends on the energy), the amount of produced scintillation light will depend on the actual absorption process. For example a one step photoelectric absorption and a two step Compton scatter with subsequent absorption will yield different amounts of scintillation light.

The above mentioned items are responsible for deviations of the actual shape of the energy spectrum in figure 4.6 compared to the ideal one (figure 4.2). The photopeak appears to be blurred and its *full width at half maximum* (FWHM) over the mean value is called the energy resolution $\Delta E/E$ of the system. It can be described by the following formula:

$$\left(\frac{\Delta(E)}{E}\right)^2 \approx \left(\frac{2.35}{\sqrt{N}}\right)^2 + \left(\frac{\Delta_{intr}(E)}{E}\right)^2 + \left(\frac{\Delta_{noise}}{E}\right)^2 \tag{4.1}$$

The first term is of statistical nature since the number of photoelectrons counted by the photodetector are underlying statistical variations. The statistics can be described by the Poisson distribution whose variance, when counting N photoelectrons is given by $\sqrt{N}$. Furthermore the energy is proportional to the number of photoelectrons $E \propto N$. Hence we get:

$$\left(\frac{\Delta E}{E}\right)_{statistic} = \frac{2.35}{\sqrt{N}} \tag{4.2}$$

The factor 2.35 arises from the conversion of standard deviation to the value at FWHM for a Gaussian distribution. The statistical contribution decreases with an increasing number of photoelectrons, hence the number of photoelectrons should be as large as possible. This can be achieved by using a scintillator with a large *light yield* (LY) and a photodetector with a high detection efficiency in the wavelength region of the scintillation light.

The second term in (4.1) represents the above mentioned intrinsic energy resolution of the used scintillator material due to its nonlinearity and inhomogenity [37, 38]. The last term comprises the noise contributions to the energy resolution; like noise that may originate from the photodetector and the readout electronics.

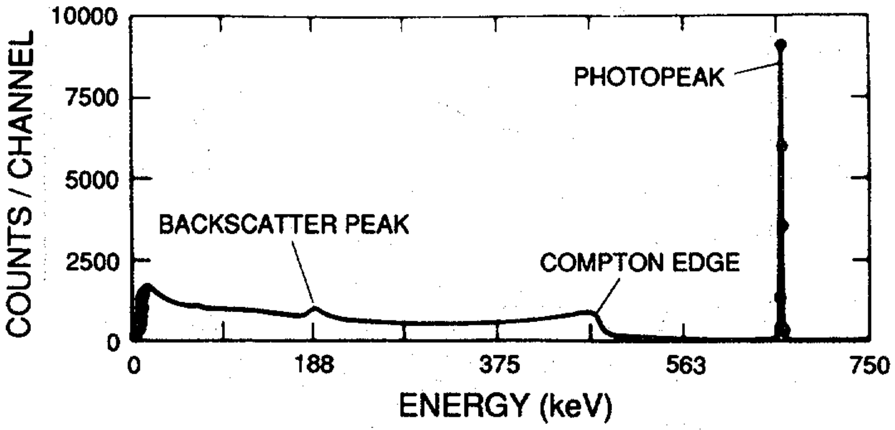

Figure 4.6: Energy spectrum of ^{137}Cs showing the full-energy photopeak (662 keV), Compton edge and the backscatter peak. [8]

4.2 Background Reduction

The main challenging part for a successful PET operation is an efficient reduction of the background events. Figure 4.7 shows three examples of events that can be classified as coincidence events; i.e. events where the arrival times of the photons fall within a small time window.

True coincidences

The figure on the left shows a coincidence event where the two gamma rays stride away from each other in anti-parallel directions. The resulting *line of response* (LOR) represents the actual situation and hence is called a “true” coincidence.

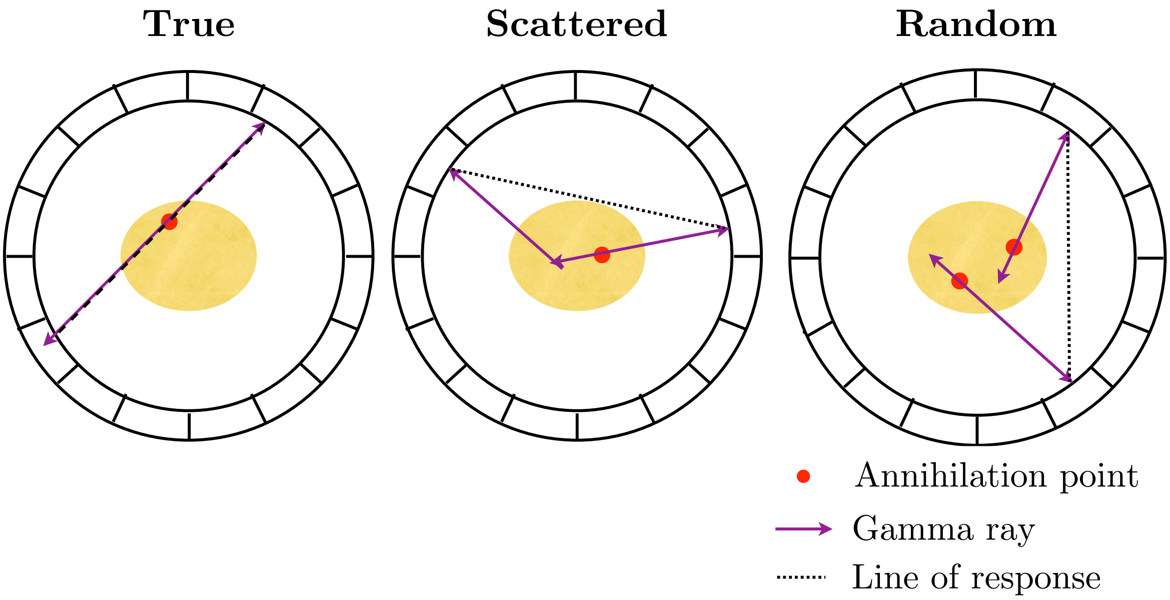

Figure 4.7: Different kinds of coincidences in a PET system. In the case of the scattered- and random-coincidences the LOR does not reflect the actual situation.

Scattered Coincidences and Energy Resolution

The picture in the middle of figure 4.7 shows a so-called “scattered” coincidence: At least one of the two annihilation photons performs a Compton scatter with an electron in the surrounding tissue where it loses a fraction of its initial energy and is diverted from its original path by an angle ϑ as it was discussed in section 1.2. The assigned LOR does not reflect the actual situation.
Scattered photons can be discriminated by measuring the energy of the detected photons precisely. A naive way to do that would be to accept only events with 511 keV energy, but as it was shown in the previous section, the photopeak is broadened and only accepting 511 keV photons would result in a huge loss of true coincidence events. Therefore it is crucial to measure the energy as precise as possible. The energy window for an accepted event

can be made smaller and hence the measured event-rate will decrease without losing true coincidences.

Random coincidence and Timing Resolution

The third event in figure 4.7 represents a random coincidence where one of the two annihilation photons was absorbed in the patient's tissue. The remaining single photons were detected and will therefore be referred to as "singles". The random rate R for a given Line of Response joining the detector elements i and j can be calculated with the following formula:

$$R = 2\tau R_i R_j \tag{4.3}$$

where τ is the coincidence time interval (typical value $\approx 10\,\mathrm{ns}$), and R_i and R_j are the single rates of detector element i and j respectively. The factor 2 appears since the effective coincidence time is 2τ. The first interaction can take place either in detector element i or in detector element j. To get the total random rate one has to sum up the individual values for each line and thus the total random rate is proportional to the hardware coincidence time window τ. A good timing resolution results in a better defined (smaller) coincidence window and therefore in a smaller random coincidence rate.

A common figure-of-merit for a PET-detector is the *Noise Equivalent Count Rate* (NECR) [39] which allows to predict the image quality depending on the true, scattered and random rates. It is defined as follows:

$$NECR = \frac{T^2}{T + S + 2R} \tag{4.4}$$

T is the true, S the scattered and R the random coincidence rate. The NECR is exactly that counting rate which would have resulted in the same signal-to-noise ratio in the data without any background (i.e. in the absence of scatter and random events). Consequently, it is always smaller than the measured rate.

The individual count rates and the NECR for different coincidence timing windows were simulated in [33] and are shown in figure 4.8 as a function of activity. One can see that the random rate decreases for a smaller coincidence window while the NECR is increasing. It shows that a small coincidence widow improves the performance of the detector. A maximum is reached at a certain activity depending on the coincidence window. Beyond this value the random-rate becomes dominant and the image quality gets worse. The chosen minimum value for the coincidence time window of $\tau_{min} = 4\,\mathrm{ns}$ is the time a photon needs to travel from one to the other side of the detector. A smaller time window would result in possible loss of true coincidences. However, this doesn't mean that there are no benefits for a smaller timing resolution. The next section describes why it is although profitable to improve timing resolution.

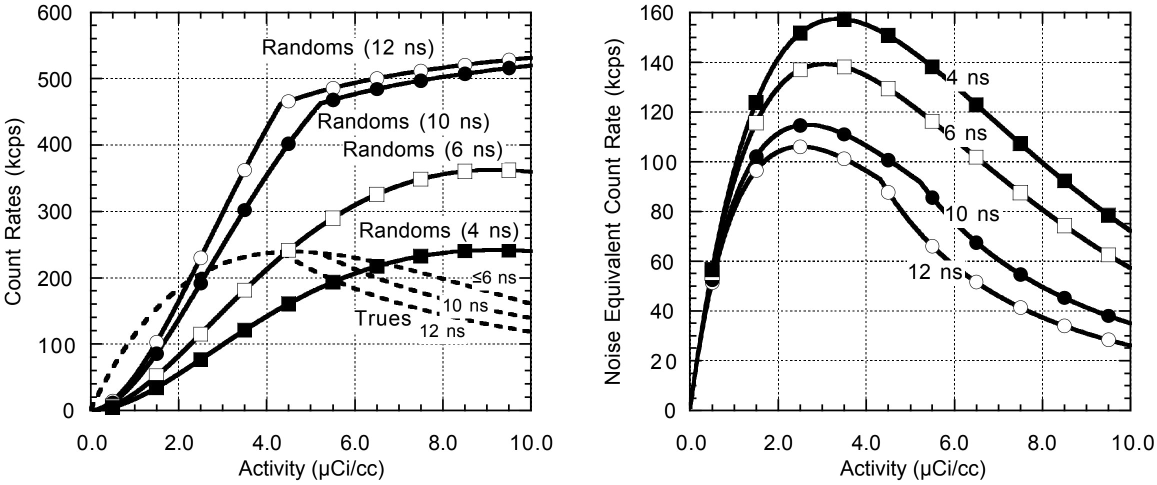

Figure 4.8: Count rates and NECR for different coincidence time windows. [33]

4.3 Time-of-Flight PET

In conventional PET the actual location of the annihilation point is unknown. It is expected to lie somewhere on the Line of Response. This situation could be changed if the difference in time $\Delta\tau$ between the arrival of the first and the second photon were known as with this information the position of the annihilation could be calculated. Assuming the situation shown in figure 4.9 we can calculate x_1 (see figure 4.9) by measuring the time difference $\Delta\tau$:

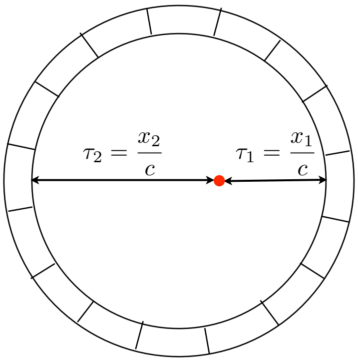

Figure 4.9: Schematic view of a PET detector for the estimation of the annihilation point by measuring the time difference. τ_1 and τ_2 are the times the photons need to travel from the annihilation point to the detector elements.

$$\Delta\tau = \tau_2 - \tau_1 = \frac{x_2 - x_1}{c}$$

Together with the knowledge about the geometry of the detector:

$$d = x_1 + x_2$$

where d is the distance between the two detector element forming the LOR (In this case the diameter).

$$\Rightarrow x_1 = \frac{d - \Delta\tau \cdot c}{2} \tag{4.5}$$

From equation 4.5 one can calculate the position error Δx as a function of the timing resolution Δt:

$$\Delta x = \frac{c}{2}\Delta t \tag{4.6}$$

Hence a timing resolution better than 50 ps would be needed to achieve a spatial resolution of $\Delta x \approx 5$ mm, which is the typical spatial resolution of a clinical PET system based on non-time-of-flight reconstruction. This number is completely out of the range of todays possibilities but it was shown in [33] that besides the reduction in the random rate and the linked improvement in the NECR, the noise variance will decrease by a factor f which can be calculated using the following formula [33]:

$$f = \frac{D}{\Delta x} = \frac{2D}{c\Delta t}, \tag{4.7}$$

where D is the size of the emission source and Δt is the timing resolution. The noise variance is the interesting quantity in this case since nowadays filtered back-projection algorithms [34] are capable of removing the mean noise contribution for every LOR. Only the noise variance will remain and therefore should be reduced. Figure 4.10 illustrates the gain when using *Time-of-Flight* TOF reconstruction. For a conventional BGO based system without TOF every pixel along a reconstructed LOR is incremented with the same probability and therefore will contribute to the noise. With TOF reconstruction the noise variance is reduced since only the pixels in the direct vicinity (given by the timing resolution) of the calculated annihilation point are incremented with a probability.

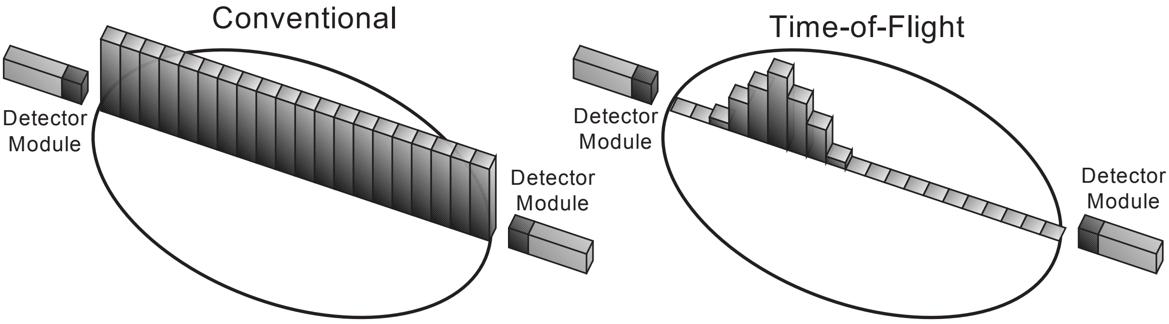

Figure 4.10: Using conventional reconstruction all pixels along the LOR are incremented with the same probability. With TOF reconstruction each pixel is incremented with a probability given by the measured time difference and the timing resolution. [33]

During the 1980's TOF PET has been extensively studied, but the negative aspects linked to the fast scintillators available at that time (BaF_2 see table 4.2) like small light yield and UV-emission yielded that this technique was not followed up. Nowadays new scintillating materials like LSO with good timing properties are available. Together with new fast photon detectors like the SiPM this could lead to new developments in TOF PET.

4.4 Experimental Setup

A two-channel setup was built at the *Deutsches Elektronen Synchrotron* (DESY) in Hamburg which allowed to measure the energy and the timing resolution when using MPPCs instead of the commonly used detectors. Prior to the PET measurements the characteristic parameters of each device were measured with a setup similar to the setup described in chapter 3. The results are shown in the following table:

Active area [mm^2]	Number of Pixels	Operating Voltage [V]	Gain [10^5]	Dark-rate 0.5pe [kHz]	Dark-rate 1.5pe [kHz]
1×1	400	76	7.4-7.5	220-250	9-10
3×3	3600	70	7.4-7.5	3200-3300	320-330

Table 4.3: Measured parameters of the used MPPCs. The dark-rate was measured at 2V over the breakdown voltage for a 0.5 photoelectron and 1.5 photoelectron threshold respectively.

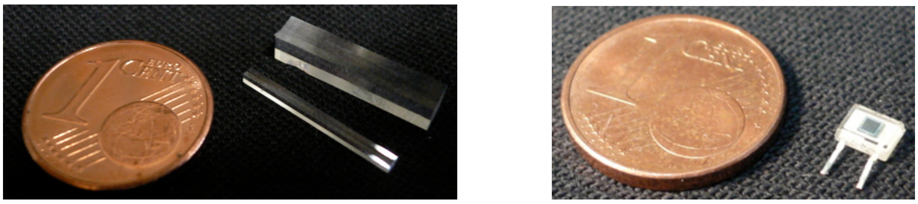

Figure 4.11: Left: Photograph of LSO crystals used for the measurement. ($1 \times 1 \times 15\,\mathrm{mm}^3$ and $3 \times 3 \times 15\,\mathrm{mm}^3$). **Right:** Photograph of one used MPPC with an active surface of $1 \times 1\,\mathrm{mm}^2$ used for the measurements.

Scintillator	Size [mm^3]	Used Detector	Detector Active Surface [mm^2]
LSO[a]	$1 \times 1 \times 15$	MPPC 400 pixels	1×1
LSO[a]	$3 \times 3 \times 15$	MPPC 3600 pixels	3×3
LFS[b]	$3 \times 3 \times 15$	MPPC 3600 pixels	3×3

---

[a] From Hilger Crystals

[b] From Lebedev Institute

Table 4.4: Scintillator crystals used for the measurement and the corresponding detectors which were used to read out the scintillation light.

Two scintillating crystals were wrapped in a few layers of teflon tape (forming a $\approx 2\,\mathrm{mm}$ thick layer) with one side left-open to attach it to the MPPC. Each of them was placed on a carrier (see figure 4.12) which could be moved in a way that it was always aligned with the counterpart on the other side. The MPPCs were attached to the crystal surface using some optical grease to increase the light yield. Figure 4.11(left) shows a picture of the unwrapped LSO crystals used for the experiment. Table 4.4 shows the dimensions of the crystals and the corresponding MPPCs which were used to detect the scintillation light.

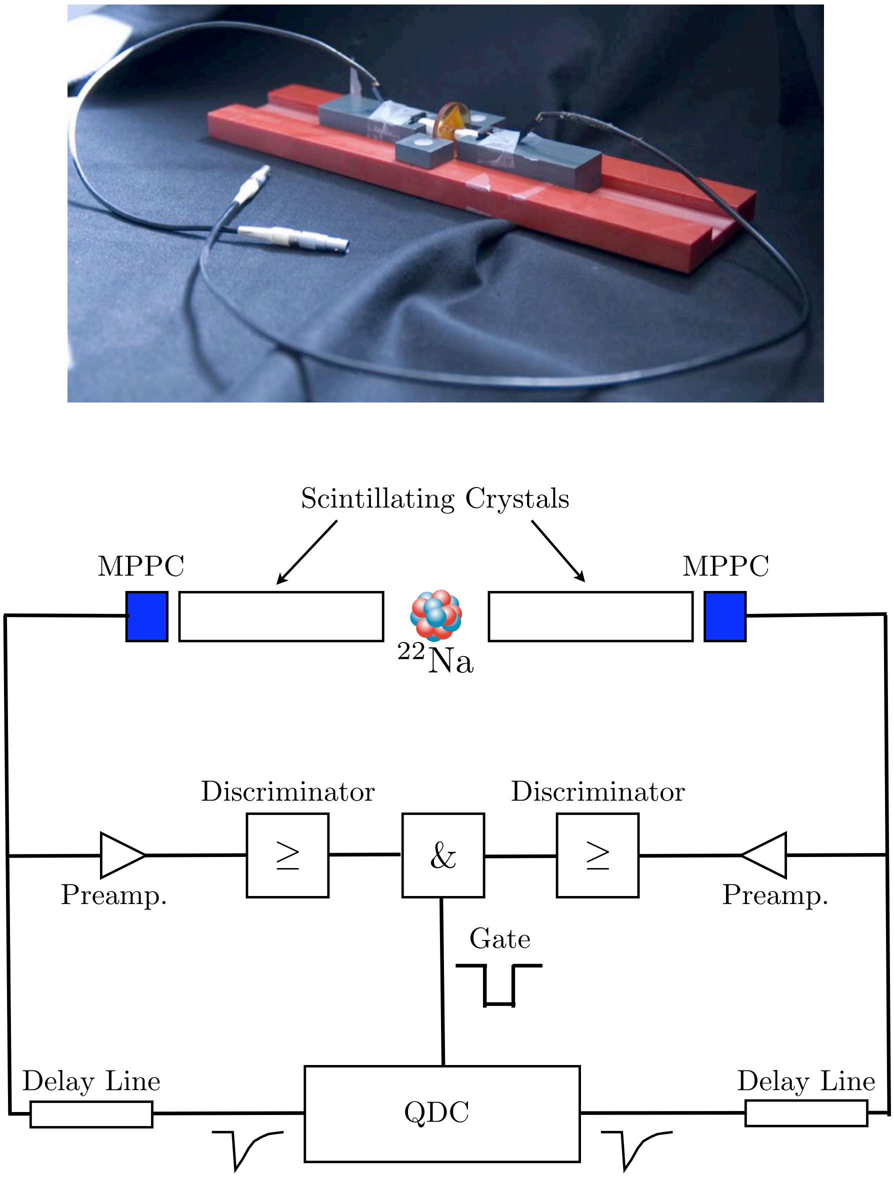

Figure 4.12: Photograph of hardware used to carry the ^{22}Na source (orange plate in the middle) and the two scintillation crystals together with a schematic drawing of the experimental setup used for the energy resolution measurements.

A point-like ^{22}Na source was placed on a fixture in between the two scintillating crystals. It decays via β^+-emission ($^{22}_{11}\text{Na} \rightarrow {}^{22}_{10}\text{Ne} + e^+ + \nu_e$) and hence is appropriate to be used as a positron source. A photograph of the fixture carrying the scintillation crystals and the β^+-source is shown in the upper part of figure 4.12. The lower part shows a schematic view of the complete setup indicating the readout electronics.

The signal from each MPPC was split into two parts: One part was guided to a QDC (LeCroy Model 1182) without being amplified. The other part (logical part) of the signal passed through a preamplifier where the voltage pulse was amplified by a factor 50 and 20, respectively. Then the pulse was guided to a threshold discriminator where a logical pulse with a width of $\mathrm{T}_{0,5} = 50\,\mathrm{ns}$ was generated if the input pulse amplitude was higher than an adjustable threshold. The generated logical pulses were guided to a logical AND-module. If two pulses arrived within the coincidence time window determined by the logical pulse width according to:

$$\mathrm{T}_{\mathrm{coincidence}} = 2 \cdot \mathrm{T}_{0,5} = 100\,\mathrm{ns}\,,$$

a gate with a length of $\mathrm{T}_{\mathrm{integration}} = 150\,\mathrm{ns}$ is generated, triggering the integration of the MPPC-signals using the QDC based on a *Versa Module Eurocard* (VME) system. Here, the size of the coincidence window was much larger than in a real PET system ($\approx 12\,\mathrm{ns}$) since this measurement was focussed on the energy resolution only. Delay lines were used to tune the arrival time of the the signal of the QDC. In this way the delay introduced by the discriminator and logical unit was compensated. The acquired data were processed on the lab computer using the software ROOT.

4.5 Energy Resolution Results

The energy resolution was systematically studied by measuring energy spectra as a function of the applied bias voltage to the MPPC. Also different scintillator geometry's and materials have been used (see Table 4.4). Three typical examples of the measured energy spectra are shown in 4.13. One can see that the results obtained with the $3 \times 3 \times 15\,\mathrm{mm}^3$ crystals are better in general than those obtained with the $1 \times 1 \times 15\,\mathrm{mm}^3$ crystals. The fraction of Compton events is higher for the smaller crystal caused by the increased probability for energy loss due to escaping photons or electrons as explained in section 4.1.

There are small peaks visible in the Compton continuum which refer to different photon interaction processes. Besides the Compton edge a small peak appears in the middle of the Compton continuum which is the so-called backscatter peak (see section 4.1).

A Gaussian fit was applied to the photopeaks in order to determine the width and the mean value of the peak. The fits and the corresponding parameters can also be seen in figure 4.13. In principle, the photopeak doesn't show an ideal Gaussian shape. Especially on the left side it is biased due to multiple Compton scattering events filling the gap between the Compton edge and the photopeak. However the parameters could be determined precisely by excluding the small area near the gap. The energy resolution is defined as the FWHM of the photo-peak over the pedestal-subtracted mean:

$$\frac{\Delta E}{E} = \frac{FWHM}{Mean - Pedestal}$$

where the pedestal value was either directly read from the energy spectrum (if possible as in figure 4.13(b)), or determined by delaying the signal in a way that only the residual noise was integrated by the QDC. The energy resolution was optimised by varying the bias voltage applied to the SiPM. Table 4.5 lists the best values obtained for the energy resolution. The error was determined by measuring the energy resolution multiple times, the obtained values varied in the range of the reproducibility. For the $1 \times 1 \times 15\,\mathrm{mm}^3$-crystals the error is much larger than for the $3 \times 3 \times 15\,\mathrm{mm}^3$-crystals. This can be explained with the rather difficult alignment of the small crystals. A small deviation from the optimal coupling position between the crystal and the MPPC results in a rather large variation of the measured number of

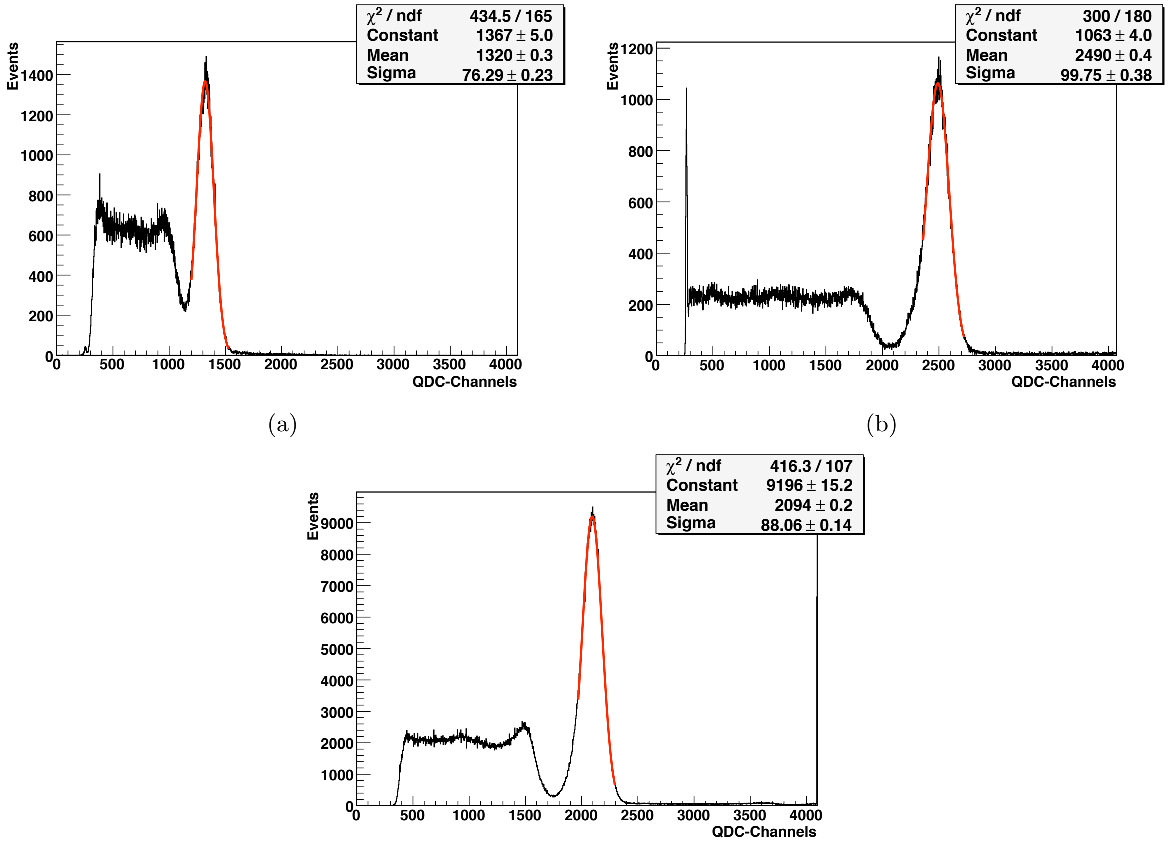

(a)

(b)

(c)

Figure 4.13: Obtained energy spectra with Gaussian fits (red) for different crystal geometry's and materials. (a): $1 \times 1 \times 15\,\mathrm{mm}^3$ LSO crystal, (b): $3 \times 3 \times 15\,\mathrm{mm}^3$ LSO crystal, (c): $3 \times 3 \times 15\,\mathrm{mm}^3$ LFS crystal

Scintillator dimensions [mm^3]	Energy Resolution [%]	Error (relative) [%]
LSO $1 \times 1 \times 15$	14	10
LSO $3 \times 3 \times 15$	10	3
LFS $3 \times 3 \times 15$	11	3

Table 4.5: Optimised values for the energy resolution.

photons. However, the results are still precise enough to show the high potential of the SiPM for the PET application. Knowing that the intrinsic energy resolution of LSO is $\Delta_{intr}(E)/E = 8,85\%$ [38] for 511 keV photons, and taking a look at equation 4.1:

$$\left(\frac{\Delta(E)}{E}\right)^2 \approx \left(\frac{2,35}{\sqrt{N}}\right)^2 + \left(\frac{\Delta_{intr}(E)}{E}\right)^2 + \left(\frac{\Delta_{noise}}{E}\right)^2$$

one may infer from the measurement that the statistical and the noise contribution are rather small. The small noise-term is expected due to the high gain of the SiPM making amplification (possible source of noise) unnecessary. The key factor yielding the small statistical term is the enhanced sensitivity in the blue wavelength region of the MPPC since the peak emission wavelength of LSO is 420 nm. An earlier study [40] using a traditional green-sensitive SiPM yielded an energy resolution of only $\approx 35\%$ due to the reduced sensitivity to blue light. The approximate values of photoelectrons for this measurement are 1200 for the $3 \times 3 \times 15\,\mathrm{mm}^3$-crystals and 300 for the $1 \times 1 \times 15\,\mathrm{mm}^3$-crystals. This value was calculated by the following formula:

$$N = \frac{Mean - Pedestal}{Gain}$$

To measure the gain, the SiPM was illuminated with a pulsed LED (see gain measurement) with the overall setup kept close to the PET setup (i.e. using the signal splitter and delay lines).

4.6 Timing Resolution Results

The measurement of the timing resolution was performed by guiding the signals from both MPPCs directly to an oscilloscope[3]. Due to the high sampling rate of the oscilloscope the intrinsic timing resolution was about 50 ps which was well suited for this application. A schematic view of the setup can be seen in figure 4.14. The measurement was carried out for the $1 \times 1 \times 15\,\mathrm{mm}^3$ LSO crystals only.
A jitter analysis software could be used to measure the time differences between the leading edges of the MPPC signals. For an idealised system and a point-like source, measuring the time difference for every coincidence event should yield always the same value, since the position of the source (i.e. the annihilation position) is fixed. However, due to contributions from the scintillation crystal and from the MPPC the measured values are underlying variations referred to as the timing resolution of the system.

For this measurement two different thresholds were defined:

1. **Trigger threshold** $N_{trigger}$: A coincidence was assumed if both MPPC signals crossed this threshold (see figure 4.15). A large value was chosen for it in order to discriminate the Compton background signals. This means it was only triggered on events above the Compton edge in figure 4.13. This represents only an approximation since it was not triggered on the energy but on the pulse amplitude assuming proportionality between these quantities (i.e. the amplitude in mV is only roughly proportional to the energy, expressed by the charge of the signal). However, it provides a raw cut on the energy

---

[3] Tektronix model 7204, 4GHz analogue bandwidth, 20Gs/s

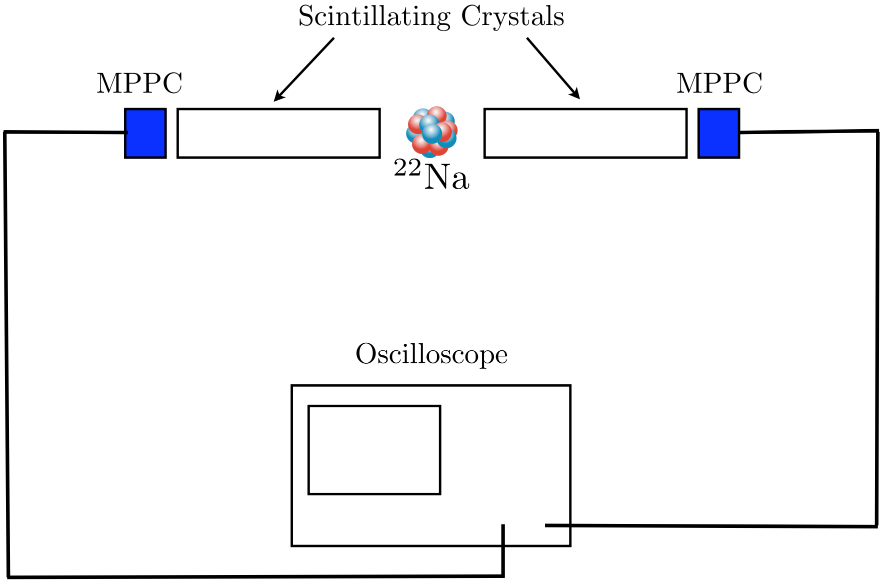

Figure 4.14: Setup for the timing measurement. The signals were directly guided to an oscilloscope for evaluation.

scale sufficient to discriminate most of the background. Figure 4.16 shows an example-event where one of the two signal pulses arises from the photoelectric absorption while the other one arises from the Compton scattering.

2. **Timing threshold** N_{timing}: The actual time difference between the two signals was not measured at the trigger threshold, but at the timing threshold. Its value is chosen as small as possible (just above the electronics noise level) since it turned out in previous measurements that the timing resolution improved with a threshold getting smaller.

Several timing resolution measurements for different trigger thresholds $N_{trigger}$ were performed. The acquired histograms are shown in figure 4.17. For a low trigger threshold of 10 mV ($N_{trigger} \approx$ 10 photoelectrons) and a timing threshold of $N_{timing} \approx 2$ photoelectrons (see figure 4.17a) a large Compton background is superimposed to the clean photoelectric events. By performing a fit which is the sum of two Gaussian functions it is possible to separate the two components. One component shows a FWHM of 700 ± 60 ps referring to the photoelectric events (signal) while the other component (referred to as background) shows a much broader distribution of $\Delta t_{10} = (1,41 \pm 0.07)$ ns. The background appears since the trigger threshold is much lower than the 300 photoelectrons of an photoelectric event, and therefore also Compton events are allowed. The Compton events show a smaller amplitude (figure 4.16) and therefore a smaller slope of the leading edge. If one pulse arises by photoelectric and the other one by Compton interaction, this will lead to another time difference compared to two photoelectric events (figure 4.15) at a constant timing threshold. Therefore the timing resolution is degraded.

If the trigger threshold is increased ($N_{trigger} \approx$ 50 photoelectrons) (figure 4.17b) the background reduces and the timing resolution is improving to $\Delta t_{50} = (650 \pm 20)$ ps. Finally, when triggering on $N_{trigger} \approx$ 70 pe (figure 4.17c), the timing resolution becomes $\Delta t_{70} = (578 \pm 35)$ ps

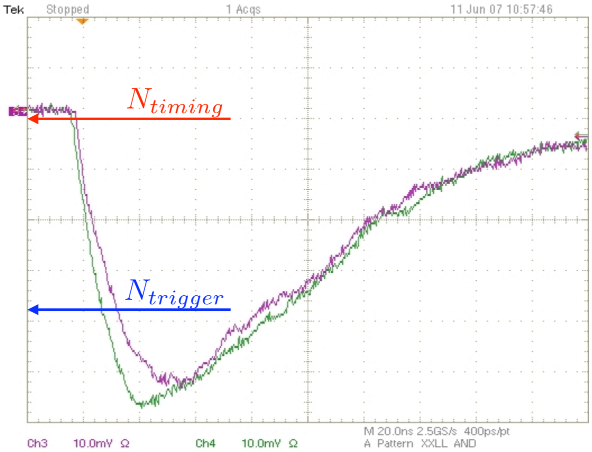

Figure 4.15: Picture of the oscilloscope display showing two photoelectric signals together with trigger and timing threshold.

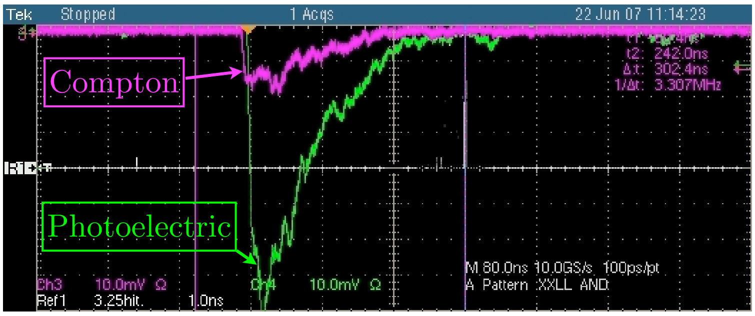

Figure 4.16: Picture of the oscilloscope display showing one photoelectric and one background event.

and no background is visible anymore. This value is close to a typical value for the timing resolution $\Delta t = 475\,\mathrm{ps}$ [41] measured with LSO and a photomultiplier tube. It was shown [33] that with a coincidence timing resolution of 500 ps (besides the benefits described in section 4.2 due to the decreased random rate), the noise variance will reduce by a factor of 5 (compared to a non TOF BGO-based camera with a 12 ns coincidence window and a 35 cm diameter object). Further studies are needed for a complete understanding of the systematic's introduced by the two thresholds $N_{trigger}$ and N_{timing}. In addition one has to take into account that this measurement was carried out with a setup containing components (e.g. the oscilloscope) which are not appropriate for a multi channel measurement. However, the results can be seen as a first demonstration of the high potential of the SiPM used under optimal conditions.

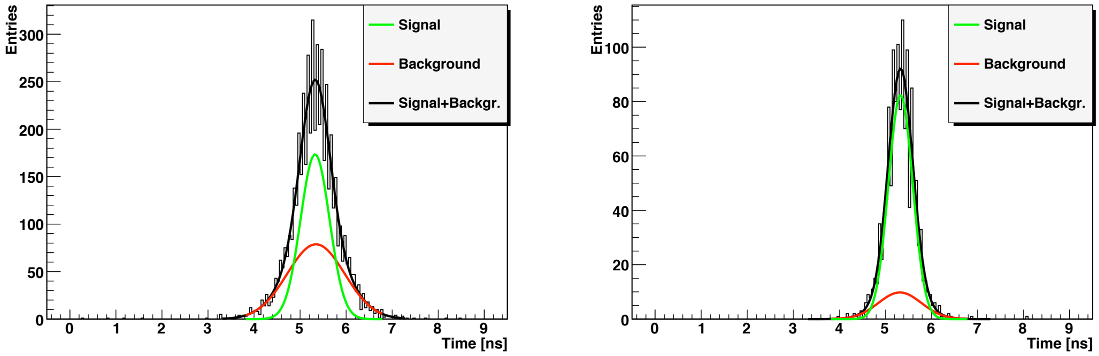

(a) Trigger threshold at ≈ 10 photoelectrons

(b) Trigger threshold at ≈ 50 photoelectrons

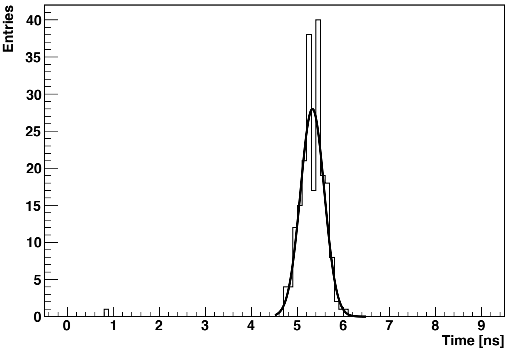

(c) Trigger threshold at ≈ 70 photoelectrons

Figure 4.17: Signal and Background of the timing resolution. The timing threshold was set for all measurements to the minimum value of 2 mV.

Chapter 5

Conclusion and Outlook

This thesis is devoted to the characterisation of the *Silicon Photomultiplier* (SiPM) which is a newly developed device suitable for low intensity light detection. In addition the application of the SiPM to the medical imaging technique of *Positron Emission Tomography* (PET) was tested.

The ILC experiment motivates the development of a highly granular sampling-calorimeter in order to match the necessary physics requirements. A prototype of this calorimeter has been built at DESY in Hamburg utilising the SiPM for the scintillation light measurement. The properties of these devices are: high detection efficiency, high gain, small size, low operation voltage, robustness and good single photon resolution.

In order to determine the characteristic properties of SiPMs, a test setup was developed and constructed in the context of this thesis which allows to measure and compare the important parameters of SiPMs with a common setup. The possibilities of the setup contain systematic measurements of the gain and the dark-rate as a function of the reverse bias voltage applied to the SiPM, as well as a measurement of the photon detection efficiency which represents one of the most important parameters of a photon detector. Eight samples with pixel numbers ranging between 100 and 1600, from two different manufacturers were tested. The measured gain values lie in a range between $M = 10^5$ up to $M = 3 \cdot 10^6$ (depending on pixel size and bias voltage). These values are comparable to values obtained for PMT's. The measured dark-rates for the one photoelectron threshold are high: $(1 - 100) \cdot 10^5\,\mathrm{Hz}$. However, it could be shown that this value decreases strongly when increasing the counting threshold. Results for the photon detection efficiency have been obtained for a MPPC with 1600 pixels. An enhanced sensitivity in the blue wavelength region was measured.

Besides the general characterisation, the application of SiPMs to PET has been studied. A two channel setup was built at DESY using the MPPC for the read-out of scintillation light. Energy and timing resolution of the system were measured. For the energy resolution, using LSO as scintillator a value of $\Delta E/E = (10 \pm 0.3)\,\%$ was measured for a crystal dimension of $3 \times 3 \times 15\,\mathrm{mm}^3$. This value is close to the relative intrinsic energy resolution of $\Delta_{intr.}/E = 8.85\%$ for 511 keV photons. For smaller crystals, the measured resolution was only slightly worse. A value of $\Delta t = (578 \pm 35)\,\mathrm{ps}$ was measured for the timing-resolution which is comparable to values obtained with photomultiplier tubes. These results demonstrate the high potential of the MPPC for the PET application.

In order to demonstrate the applicability of the concept in PET (e.g. to study the spatial resolution), the construction of a small prototype is planned for the future. A solution for a multi channel readout which can be scaled to large channel numbers is one of the main challenges.

The functionality of the test-setup was proven. However, the characterisation measurements could be complemented by more systematic studies of the dependency of the PDE on the applied reverse bias voltage. In addition, the study of the properties of a series of devices, identical in construction is planed, in order to make statements about the “device to device”-uniformity (e.g. variations of the breakdown-voltage). A high uniformity is in particular advantageous for PET and ILC applications since variations in U_{break} make the development of readout electronics for a huge number of channels difficult.

Appendix A

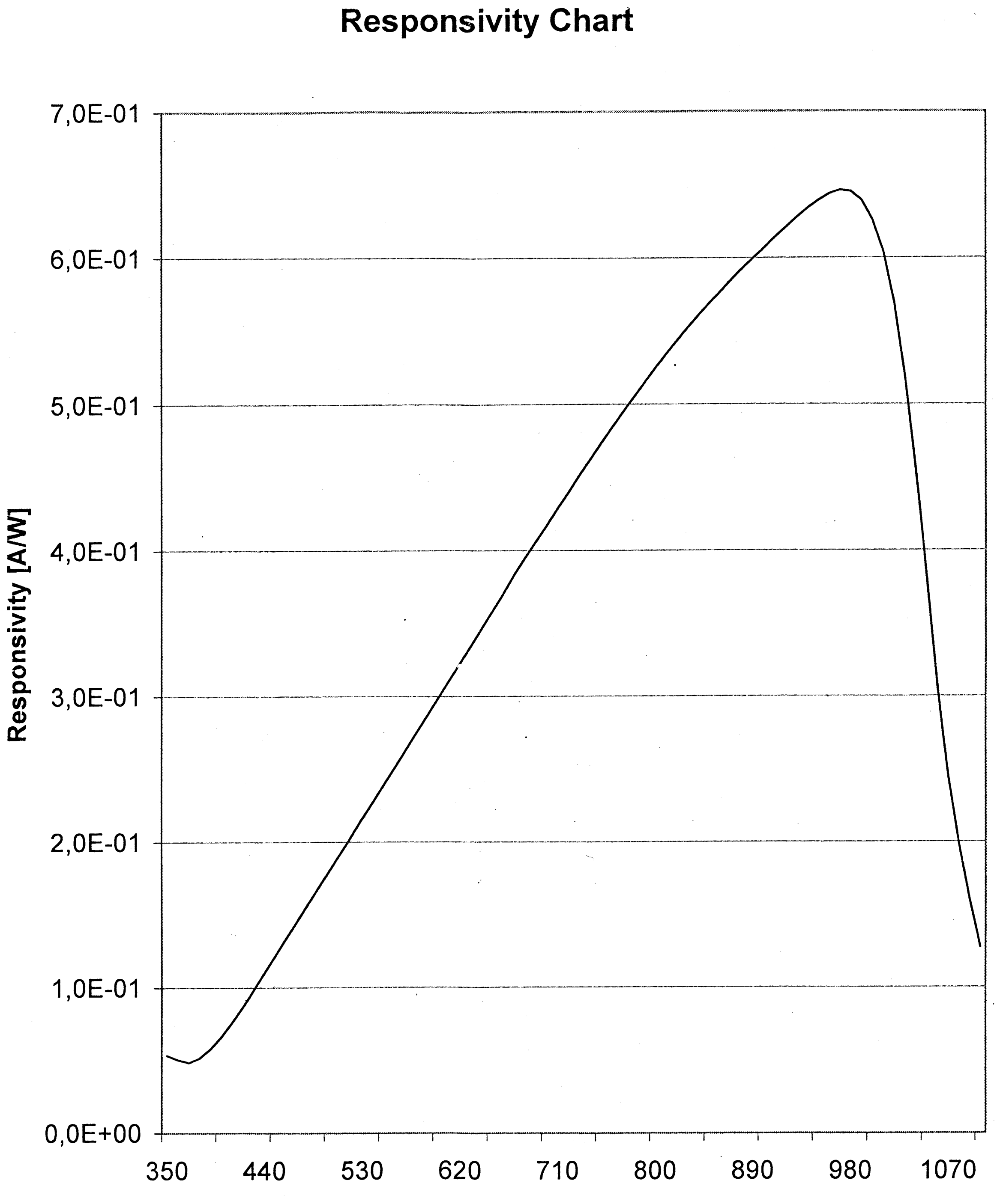

Figure A.1: Responsivity of the calibrated PIN-diode.

Bibliography

[1] Ilc reference design report, August 2007.

[2] William W. Moses, editor. *SYNERGIES BETWEEN ELECTROMAGNETIC CALORIMETRY AND PET*. Lawrence Berkley National Laboratory, 2002.

[3] P. E. Vert, J. Lecoq, G. Montarou, N. Pauna, B. Joly, M. Boutemeur, H. Mathez, R. Gaglione, and P. Le Du. Contribution of high energy physics techniques to the medical imaging field, 2006.

[4] The SiD-group. Sid detector outline document, May 2006.

[5] The LDC-group. Detector outline document for the large detector concept, August 2006.

[6] The GLD-group. Gld detector outline document, October 2006.

[7] The 4th concept group. Detector outline document for thefourth concept detector (“4th”) at the international linear collider, August 2006.

[8] G. Nelson and D. Reilly. Gamma-ray interactions with matter.

[9] Passage of particles through matter. Particle Data Group.

[10] Claus Grupen. *Teilchedetektoren*. BI Wissenschaftsverlag, 1993.

[11] J.-C. Brient, P. Dauncey, E. Garutti, I. Laktineh, R. Poeschl, J. Repond, F. Sefkow, T. Takeshita, D. Ward, and J. Yu. Calice report to the calorimeter r&d review panel, 2007.

[12] Nanda Wattimena. The calice tile hadron calorimeter prototype with silicon photomultiplier readout. In *10th ICATPP Conference on Astroparticle, Particle, Space Physics, Detectors and Medical Physics Applications*, 2007.

[13] V. Andreev, J. Cvach, M. Danilov, E. Devitsin, V. Dodonov, G. Eigen, E. Garutti, Yu. Gilitzky, M. Groll, R. D. Heuer, M. Janata, I. Kacl, V. Korbel, V. Kozlov, H. Meyer, V. Morgunov, S. Nemecek, R. Poschl, I. Polak, A. Raspereza, S. Reiche, V. Rusinov, F. Sefkow, P. Smirnov, A. Terkulov, S. Valkar, J. Weichert, and J. Zalesak. A high-granularity plastic scintillator tile hadronic calorimeter with apd readout for a linear collider detector. *Nuclear Instruments and Methods in Physics Research Section A: Accelerators, Spectrometers, Detectors and Associated Equipment*, 564(1):144–154, 2006.

[14] V. Andreev, V. Balagura, B. Bobchenko, P. Buzhan, J. Cvach, M. Danilov, E. Devitsin, V. Dodonov, B. Dolgoshein, G. Eigen, L. Filatov, E. Garutti, M. Groll, R. D. Heuer, A. Ilyin, M. Janata, I. Kacl, V. Kantserov, V. Kaplin, A. Karakash, S. Klemin, V. Korbel,

V. Kozlov, H. Meyer, R. Mizuk, V. Morgunov, E. Novikov, S. Nemecek, R. Poschl, I. Polak, E. Popova, A. Raspereza, S. Reiche, V. Rusinov, F. Sefkow, P. Smirnov, S. Smirnov, Yu. Soloviev, E. Tarkovsky, A. Terkulov, V. Tikhomirov, S. Valkar, J. Weichert, and J. Zalesak. A high-granularity scintillator calorimeter readout with silicon photomultipliers. *Nuclear Instruments and Methods in Physics Research Section A: Accelerators, Spectrometers, Detectors and Associated Equipment*, 540(2-3):368–380, 2005.

[15] N. D'Ascenzo, A. Eggemann, and E. Garutti. Study of micro pixel photon counters for a high granularity scintillator-based hadron calorimeter, 2007.

[16] V. Saveliev and V. Golovin. Silicon avalanche photodiodes on the base of metal-resistor-semiconductor (mrs) structures. *Nuclear Instruments and Methods in Physics Research Section A: Accelerators, Spectrometers, Detectors and Associated Equipment*, 442(1-3):223–229, 2000.

[17] P. Buzhan et al. An advanced study of silicon photomultiplier. *ICFA Instrum. Bull.*, 23:28–41, 2001.

[18] Kwok K. Ng. *Complete Guide to Semiconductor Devices.* Wiley, 2002.

[19] Gerhard Lutz. *Semiconductor Radiation Detectors.* Springer, 1999.

[20] B.K.Lubsandorzhiev. On the history of photomultiplier tube invention. *Nucl.Instrum.Meth.*, A(567):236–238, 2006.

[21] Optical properties of silicon. http://www.udel.edu/igert/pvcdrom/index.html.

[22] HAMAMATSU. *Technical Information: Characteristics and use of Si APD (Avalanche Photodiodes)*, May 2004.

[23] HAMAMATSU. *Photodiode Technical Information.*

[24] R. J. McIntyre. Theory of microplasma instability in silicon. *Journal of Applied Physics*, 32(6):983–995, 1961.

[25] Brian F. Aull, Andrew H. Loomis, Douglas J. Young, Bradley M. Heinrichs, Richard J. Felton, Peter J. Daniels, and Deborah J. Landers. Geiger-mode avalanche photodiodes for three- dimensional imaging. *LINCOLN LABORATORY JOURNAL*, 13(2):335–350, 2002.

[26] Claudio Piemonte. A new silicon photomultiplier structure for blue light detection. *Nuclear Instruments and Methods in Physics Research Section A: Accelerators, Spectrometers, Detectors and Associated Equipment*, 568(1):224–232, 2006.

[27] J. Barral. Study of silicon photomultipliers. Master's thesis, Ecole Polytechnique, France, 2004.

[28] A. G. Chynoweth and K. G. McHay. Photon emission from avalanche breakdown in silicon. *Physical Review*, 102(2):369–376, April 1956.

[29] A. Lacaita, S. Cova, A. Spinelli, and F. Zappa. Photon-assisted avalanche spreading in reach-through photodiodes. *Appl. Phys. Lett.*, 62(6):606–608, February 1993.

[30] Jeff Bude, Nobuyuki Sano, and Akira Yoshii. Hot-carrier luminescence in si. *Physical Review B*, 45(11):5848–5856, March 1992.

[31] Valeri Saveliev. Eudet jra3, activity. Presentation, December 2005.

[32] Kenneth S. Krane. *Introductory nuclear physics.* Wiley, New York [u.a.], 1988.

[33] William W. Moses. Advantages of improved timing accuracy in pet cameras using lso scintillator. *Nuclear Science Symposium Conference Record*, 3:1670–1675, November 2002.

[34] Dale L.Bailey David W. Townsend Peter E. Valk Michael N. Maisey. *Positron Emission Tomography.* Springer, 2005.

[35] N. D'Ascenzo, E. Garutti, M. Goettlich, H.C. Schultz-Coulon, and A. Tadday. Study of micro pixel photon counter for the application to positron emission tomography. *To be published in NIM*, 2008.

[36] J.S. Melcher, C.L.; Schweitzer. Cerium-doped lutetium oxyorthosilicate: a fast, efficient newscintillator. *Nuclear Science, IEEE Transactions on*, 39(4):502–505, August 1992.

[37] M. Balcerzyk, M. Moszynski, W. Mengesha, J.D Valentine, and W. Klamra. Intrinsic energy resolution and nonlinearity of some contemporary scintillators. -, -.

[38] M. Balcerzyk M. Moszynski Mkapusta D. Wolski J. Pawelke C. L. Melcher. Yso, lso, gso and lgso. a study of energy resolution and nonproportionality. *IEEE Transactions on Nuclear Science*, 47(4), August 2000.

[39] Strother S.C. Casey M.E. Hoffman E.J. Measuring pet scanner sensitivity: relating countrates to imagesignal-to-noise ratios using noise equivalents counts. *Nuclear Science, IEEE Transactions on*, 37(7):783–788, April 1990.

[40] D.J. Herbert et al. Study of sipm as a potential photodetector for scintillator readout. *NUCLEAR INSTRUMENTS AND METHODS IN PHYSICS RESEARCH SECTION A*, 567(1):356–359, 2007.

[41] S. E. Derenzo W. W. Moses. Prospects for time-of-flight pet using lso scintillator. *IEEE Transactions on Nuclear Science*, 46:474–478, 1999.

Danksagungen

Ich möchte mich bei folgenden Personen für Ihre Unterstützung bei dieser Arbeit bedanken.
An erster Stelle bedanke ich mich bei Herrn Prof. Dr. Hans-Christian Schultz-Coulon und bei Frau Dr. Erika Garutti für das Ermöglichen dieser Diplomarbeit und für die gute Betreuung.
Herrn Professor Dr. Markus Oberthaler danke ich für die Bereitschaft diese Arbeit als Zweitgutachter zu lesen.
Mein Dank gilt auch Dr. Rainer Stamen, für die Betreuung, das ständige zur Verfügung stehen für meine Fragen sowie für das geduldige Korrekturlesen dieser Arbeit.
Mein besonderer Dank geht an Nicola D'Ascenzo für die freundschaftliche Betreuung währed der Zeit am DESY in Hamburg, sowie für das vermittelte Wissen, die guten Ideen und für das Korrekturlesen zum Schluss.
Desweiteren möchte ich mich bei Herrn Dr. Jürgen Stiewe für das lesen der Arbeit und für die Korrekturvorschläge bedanken.
Den weiteren Mitgliedern der ILC Forschungsgruppe am KIP möchte ich ebenfalls danken: Bei Alexander Kaplan möchte ich mich im speziellen für die Hilfe beim Einrichten der Data-acquisition und bei Wei Shen für seine Hilfe bei Fragen zur Elekronik bedanken.
Der Elektronikabteilung des KIP, im besonderen Klaus Schmitt und Peter Stock danke ich für die guten Ratschläge während des Aufbaus des Setups.
Bedanken möchte ich mich auch bei der gesamten ATLAS Gruppe des KIP: Felix Müller, Frederik Rühr, Dr. Victor Lendermann, Dr. Florian Föhlisch, Dr. Pavel Weber, Michael Henke, Christoph Anders, Dr. Jochen Dingfelder, Dr. Martin Wessels, Michel Janus, Dr. Rainer Stamen, Dr. Taylor Childers, Bernd Amend, Ion Stroescu, Veit Scharf und Victor Andrei für die unkomplizierte Hilfe bei Problemen, und vor allem für die gute Stimmung und die tolle Zeit beim Grillen und Kubb spielen.

Ein ganz besonderer Dank geht zum Schluss an meine Familie und meine Freundin Stephanie, die mich während des gesamten Studiums begleitet hat und mich in den anstrengenden Zeiten motivierte.
Vielen Dank!

Erklärung:

Ich versichere, dass ich diese Arbeit selbstständig verfasst und keine anderen als die angegebenen Quellen und Hilfsmittel benutzt habe.

Heidelberg, den 13.02.2008

Unterschrift